CRYSTAL GROWTH & DESIGN

pubs.acs.org/crystal

Article

Layered Inorganic–Organic 3,5-Dimethylpyrazole-4-Sulfonate Films for Protection of Copper Surfaces against Corrosion

Wisam A. Al Isawi, Sarut Jianrattanasawat, Eleftherios Tripodianos, Konstantinos D. Demadis,* Alexander M. Kirillov, Matthias Zeller, and Gellert Mezei*

Cite This: *Cryst. Growth Des.* 2021, 21, 5421–5439

Read Online

ACCESS | Metrics & More | Article Recommendations | Supporting Information

ABSTRACT: A series of 11 compounds, including alkali (Li, Na, K, Rb, Cs) and alkaline-earth (Mg, Ca, Sr, Ba) coordination polymers, transition-metal (Cu, Cd) complexes, and the ammonium salt of 3,5-dimethylpyrazole-4-sulfonic acid (HL), were synthesized. Single crystals of $HL{\cdot}H_2O$, $LiL(H_2O)$, $NaL(H_2O)$, RbL, CsL, $CaL_2(H_2O)$, $SrL_2(H_2O)$, $BaL_2(H_2O)$, $CuL_2(H_2O)_3{\cdot}2.3H_2O{\cdot}0.5$(acetone), and $CdL_2(H_2O)_3{\cdot}2H_2O$ were obtained from aqueous solutions either by evaporation or acetone vapor diffusion. Characterization by single-crystal X-ray diffraction reveals that the coordination compounds of L^- (except Cu) possess alternating inorganic–organic layered structures, in which L^- engages in extensive charge-assisted networks of H-bonding and aromatic interactions as well as metal coordination through the pyrazole N atom and/or the sulfonate O atom. A topological analysis and classification of underlying metal–organic or hydrogen-bonded networks uncover a number of distinct topological nets (**3,5L2**, **hcb**, **6,6L1**, **3,5C1**, **3,8L28**, **hex**, and **pcu**). A thermogravimetric analysis shows that HL and NH_4L are stable up to 285 and 90 °C, respectively, whereas the anhydrous metal compounds decompose above 200–230 °C. The pK_a values of 3,5-dimethylpyrazole-4-sulfonic acid (HL) and pyrazole-4-sulfonic acid were determined by ^1H NMR titrations with H_2SO_4. Copper corrosion experiments indicate that 3,5-dimethylpyrazole-4-sulfonic acid (HL) is a better anticorrosion agent than the parent pyrazole-4-sulfonic acid at pH 4, whereas the coordination polymers of L^- offer weaker corrosion protection in comparison to the corresponding pyrazole-4-sulfonate complexes. The latter result is corroborated by the less compact and less robust thin films formed by metal–L compounds, as indicated by scanning electron microscopy/energy dispersive X-ray spectroscopy (SEM/EDS) measurements, and the weaker acidity of HL, which allows for easier protonation of the conjugate base L^- in metal–L compounds.

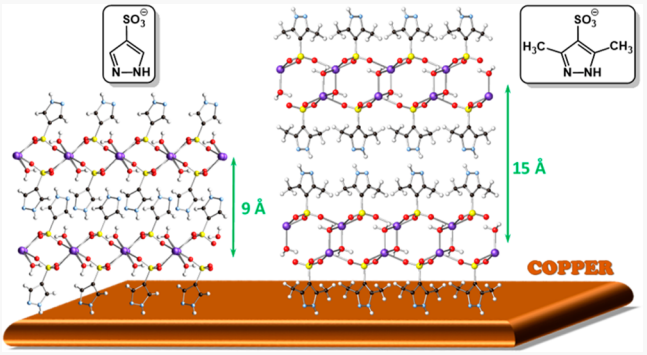

INTRODUCTION

Copper metal has been in use by humanity for more than 10,000 years and it is estimated that every person born in the United States will use on average about 950 pounds of copper in their lifetime.[1] Although it is a highly corrosion resistant metal under near pH-neutral conditions, copper surfaces become ever more susceptible to corrosion in solutions of increasing acidity or alkalinity. Corrosion is further promoted by oxygen and chloride ions, commonly present in water.[2,3] Corrosion of metals in general is a considerable problem: in the U.S. alone, the annual direct cost of metallic corrosion is $276 billion, which represents over 3% of the gross domestic product (GDP).[4] Therefore, the improved protection of metallic copper surfaces against corrosion in aqueous media (e.g., heat exchanger components in cooling water systems, post chemical–mechanical polishing cleaning) is an important area of both fundamental and applied research.[5−16]

Additives used as copper corrosion inhibitors in aqueous media contain donor atoms such as N or S, through which the inhibitor molecules anchor to copper and ultimately form a protective layer on the metal surface.[17−24] The most efficient class of inhibitors is heterocyclic aromatic compounds,[25−32] with benzotriazole and tolyltriazole (and its alkyl derivatives) being the most popular.[33−37] Pyrazole-based compounds have also been studied as copper corrosion inhibitors, but to a lesser extent.[38−40]

We have shown that pyrazole-4-sulfonate complexes of various metals form protective films on copper surfaces and provide protection against corrosion.[41,42] Pyrazole-4-sulfonic acid was also found to have anticorrosion properties on iron surfaces.[43] Structural analyses of the metal complexes, which

Received: June 14, 2021
Revised: July 23, 2021
Published: August 5, 2021

https://doi.org/10.1021/acs.cgd.1c00683
Cryst. Growth Des. 2021, 21, 5421–5439

consist of alternating inorganic/organic layers, revealed that pyrazole-4-sulfonate is an extremely versatile ligand, due to the coordination flexibility of the sulfonate group and the ability of the pyrazole moiety to participate in H-bonding, aromatic interactions, and coordination with metals. Aryl sulfonate ligands have been found to be useful for the construction of various layered solids and metal−organic frameworks[44−47] and continue to receive attention due to various applications such as CO_2 capture and conversion,[48,49] luminescent materials,[50,51] and dyes.[52−56]

Herein we report results of studies using the 3,5-dimethyl derivative of pyrazole-4-sulfonic acid, including single-crystal X-ray crystallography and thermogravimetry of various coordination polymers and metal complexes, corrosion studies of copper surfaces, and studies of the protective films by scanning electron microscopy and energy dispersive X-ray spectroscopy (SEM/EDS). Also, we report the pK_a values of both pyrazole-4-sulfonic acid and 3,5-dimethylpyrazole-4-sulfonic acid in H_2O, determined by ^{1}H NMR titrations. These studies explore the effect of the methyl substituents on the crystal structure and morphology of the protective films, and ultimately on the anticorrosion efficiency of the novel coordination polymers and metal complexes.

EXPERIMENTAL SECTION

Materials and Methods. All commercially available reagents and solvents were used as received. NMR spectra were recorded on a Jeol JNM-ECZS400 instrument at room temperature. Samples for TGA analysis were dried under high vacuum for 12 h prior to measurement with a TGA Q500 Thermal Analyzer instrument (heated at 10 °C min^{-1} from 25 to 700 °C under N_2).

Synthesis of 3,5-Dimethylpyrazole-4-sulfonic Acid Monohydrate (HL·H_2O). Because the more recently reported, one-step method[57] to prepare HL was shown to yield a product contaminated with side products,[58] the original two-step method[59] was employed. In an ice bath, 3,5-dimethylpyrazole (3.000 g, 31.21 mmol) was carefully dissolved in 10 mL of fuming sulfuric acid (20% SO_3). The resulting yellow solution was heated to 65 °C for 6 h. The cooled solution was slowly added to water (250 mL) with stirring, and barium hydroxide (59.5 g) was added slowly to neutralize the sulfonic acid product and the excess sulfuric acid. Then, a dilute solution of sulfuric acid was added dropwise into the solution to remove excess barium ions. The addition was continued until no more precipitation of $BaSO_4$ was observed. After the $BaSO_4$ was filtered off, the solution was evaporated in a rotavap and the product was purified by recrystallization from water/ethanol. Yield: 3.82 g (69%). ^{1}H NMR (400 MHz, D_2O): δ 2.35 (s, 6H, CH_3) ppm (Figure S1).

Synthesis of Coordination Polymers and Metal Complexes. 3,5-Dimethylpyrazole-4-sulfonate derivatives were prepared in quantitative yield by evaporating aqueous solutions containing stoichiometric amounts of HL·H_2O and a metal oxide (Mg^{2+}, Cu^{2+}, Cd^{2+}), metal carbonate (Li^+, Na^+, K^+, Rb^+, Cs^+, Ca^{2+}, Sr^{2+}, Ba^{2+}), or NH_3 (28% in H_2O).

pK_a Measurements. The pK_a values in H_2O of pyrazole-4-sulfonic acid or 3,5-dimethylpyrazole-4-sulfonic acid were determined at a concentration of 0.100 M by ^{1}H NMR titrations with sulfuric acid, on the basis of established procedures[60,61] using a previously reported acidity function (H).[62,63] H_2SO_4 (96.16%) was standardized using a NaOH solution (standardized with potassium hydrogen phthalate) and was used to prepare 5.000% and 0.5000% stock solutions by dilution with H_2O. Tetramethylammonium chloride (TMACl) was used as an internal standard. Solutions of pyrazole-4-sulfonic acid or 3,5-dimethylpyrazole-4-sulfonic acid (0.100 M in H_2O) containing 0.06 M TMACl and varying amounts of H_2SO_4 were prepared using either neat H_2SO_4 (96.16%) or one of the two stock solutions (depending on the concentration needed) and a 3.000 M stock solution of TMACl. A 600 μL portion of each of these solutions was transferred to an NMR tube, and the corresponding ^{1}H NMR spectra were recorded at 25 °C. To eliminate the effect of the medium on the observed chemical shifts, differences (Δ) between the chemical shifts of the substrate (aromatic C−H for pyrazole-4-sulfonic acid or methyl C−H for 3,5-dimethylpyrazole-4-sulfonic acid) and the TMACl internal standard were used for calculations. The various H_2SO_4 concentrations employed, the corresponding values of acidity functions, and the average chemical shift differences (averages of six runs) are summarized in Tables S1 and S2. Sigmoidal curves were obtained by plotting Δ vs the acidity function (Figures S2 and S3), the inflection points of which correspond to the pK_a (pK_{BH}) of the sulfonic acid (BH). To determine the pK_a values more accurately, log Q = log([BH]/[B$^-$]) = log[(Δ − Δ_B−)/(Δ_{BH} − Δ)] (where Δ_B− is the difference between chemical shifts in ppm of the ionized sulfonic acid and TMACl reference, and Δ_{BH} is the difference in chemical shifts in ppm of the un-ionized sulfonic acid and TMACl reference) was plotted against the acidity function (Figures S4 and S5). The intercepts of the resulting straight lines (log Q = $-H$ + pK_a) give pK_a values of −0.04 ± 0.01 and 1.06 ± 0.03 for pyrazole-4-sulfonic acid and 3,5-dimethylpyrazole-4-sulfonic acid, respectively.

Corrosion Inhibition Protocols. A modified protocol based on the National Association of Corrosion Engineers (NACE) Standard TM0169-95 was employed.[64] Corrosion specimens (copper metal, grade 99.999%, 1 mm thin foil) were cut into 2 × 2 cm squares and prepared according to the well-established protocol mentioned above. Each specimen was immersed in a control aqueous solution (no inhibitor) or in a test solution (0.50 mM in L or metal−L complex) at pH 2.0, 3.0, or 4.0 (adjusted with HCl), respectively, and the corrosion progress was monitored by visual inspection for a number of days. The duration of the corrosion experiments was variable. For example, for the experiments at pH 2, the duration was ∼4 days, at pH 3 it was 14−18 days (depending on individual experiment), and at pH 4 it was 18−19 days (depending on the individual experiment). Longer experiment times were required for the pH 3 and 4 experiments because copper corrosion becomes considerably slower at higher pH values. Then, the specimens were removed from the solution, surface samples were taken for spectroscopic studies, and the corrosion products were cleaned off the copper surface by the standard NACE method referenced above in order to determine corrosion rates based on mass loss. The experimental error for this technique was ±5%. Because the aforementioned method was destructive, the same set of corrosion experiments was repeated and the intact copper specimens were used for optical microscopy, scanning electron microscopy (SEM), and energy dispersive X-ray spectroscopy (EDS) studies.

X-ray Crystallography. Crystals suitable for X-ray diffraction were obtained either by slow evaporation of aqueous solutions (Na^+, Rb^+, Ca^{2+}, Ba^{2+}) or by vapor diffusion of acetone into aqueous solutions (HL, Li^+, Cs^+, Sr^{2+}, Cu^{2+}, Cd^{2+}). X-ray diffraction data were collected with a Bruker SMART APEX II diffractometer using graphite-monochromated Mo Kα (λ = 0.71073 Å) radiation, either at 100 K from a single crystal mounted atop a glass fiber under Paratone-N oil or at room temperature in the case of the Ca^{2+} compound, which was mounted using cyanoacrylate glue. The data were integrated using SAINT[65] and scaled and corrected for absorption and other effects using either SADABS[66] or TWINABS.[67] The structures were solved by employing direct methods using ShelXS[68] and refined by full-matrix least squares on F^2 using ShelXL.[69] All non-H atoms were refined with independent anisotropic displacement parameters. C−H hydrogen atoms were placed in idealized positions and refined using the riding model, whereas O−H hydrogen atoms were located from the difference Fourier maps; hydrogen displacement parameters were refined as isotropic and fixed to be 50% or 20% larger than those of the attached C or O atoms.

Crystals of both $CaL_2·H_2O$ and $BaL_2·H_2O$ were found to be nonmerohedrally twinned. In each case, the orientation matrices for the two components were identified using the program CELL_NOW,[70] with the two components being related by a 180° rotation around the reciprocal c axis (Ca) or the real a axis (Ba). The

https://doi.org/10.1021/acs.cgd.1c00683
Cryst. Growth Des. 2021, 21, 5421−5439

Table 1. Crystallographic Data

	$HL{\cdot}H_2O$	$LiL(H_2O)$	$NaL(H_2O)$	RbL	CsL
formula	$C_5H_{10}N_2O_4S$	$C_5H_9LiN_2O_4S$	$C_5H_9N_2NaO_4S$	$C_5H_7N_2O_3RbS$	$C_5H_7CsN_2O_3S$
FW	194.21	200.14	216.19	260.66	308.10
cryst syst	triclinic	orthorhombic	monoclinic	monoclinic	monoclinic
space group	$P\bar{1}$	*Aba*2	$P2_1/c$	*C*2/*m*	*C*2/*m*
a (Å)	7.2894(3)	11.2753(2)	15.8028(2)	10.2852(2)	10.6092(2)
b (Å)	7.7014(4)	28.3512(6)	5.5633(1)	5.7874(1)	5.9631(1)
c (Å)	8.7391(4)	5.5200(1)	10.6442(1)	14.6822(3)	14.7689(2)
α (deg)	87.784(3)	90.000	90.000	90.000	90.000
β (deg)	68.734(3)	90.000	107.414(1)	109.596(1)	109.040(1)
γ (deg)	65.531(2)	90.000	90.000	90.000	90.000
V (Å^3)	412.52(3)	1764.57(6)	892.90(2)	823.33(3)	883.22(3)
Z	2	8	4	4	4
D_{calc} (g·cm^{-3})	1.564	1.507	1.608	2.103	2.317
μ (mm^{-1})	0.371	0.348	0.394	6.233	4.398
θ range (deg)	2.52−25.24	2.31−26.68	2.70−36.31	1.47−30.51	2.92−30.53
no. of rflns collected	14002	10507	20568	12331	5341
R_{int}	0.0527	0.0551	0.0286	0.0328	0.0212
no. of obsd rflns ($I > 2\sigma(I)$)	1798	1558	3648	1210	1321
no. of data/restraints/params	2045/2/117	1852/4/129	4304/0/120	1381/1/93	1468/1/93
GOF (on F^2)	1.096	1.069	1.044	1.047	1.068
R factors ($I > 2\sigma(I)$)	R1 = 0.0437	R1 = 0.0318	R1 = 0.0292	R1 = 0.0187	R1 = 0.0195
	wR2 = 0.1192	wR2 = 0.0769	wR2 = 0.0785	wR2 = 0.0459	wR2 = 0.0398
R factors (all data)	R1 = 0.0496	R1 = 0.0402	R1 = 0.0371	R1 = 0.0242	R1 = 0.0415
	wR2 = 0.1245	wR2 = 0.0815	wR2 = 0.0833	wR2 = 0.0481	wR2 = 0.0481
max peak/hole (e Å^{-3})	0.801/−0.726	0.252/−0.299	0.548/−0.532	0.603/−0.508	0.467/−0.715
CCDC no.	2088836	2088838	2088839	2088840	2088841

	$CaL_2(H_2O)$	$SrL_2(H_2O)$	$BaL_2(H_2O)$	$CuL_2(H_2O)_3{\cdot}2.3H_2O{\cdot}0.5(C_3H_6O)$	$CdL_2(H_2O)_3{\cdot}2H_2O$
formula	$C_{10}H_{16}CaN_4O_7S_2$	$C_{10}H_{16}N_4O_7S_2Sr$	$C_{10}H_{16}BaN_4O_7S_2$	$C_{11.50}H_{27.69}CuN_4O_{11.84}S_2$	$C_{10}H_{24}CdN_4O_{11}S_2$
FW	408.47	456.01	505.73	539.24	552.85
cryst syst	triclinic	orthorhombic	monoclinic	triclinic	triclinic
space group	$P\bar{1}$	*Cmcm*	*C*2/*c*	$P\bar{1}$	$P\bar{1}$
a (Å)	5.5433(15)	5.3487(1)	5.2805(4)	8.5013(2)	7.9624(3)
b (Å)	11.088(2)	10.6760(2)	11.1111(7)	10.1085(2)	10.1862(4)
c (Å)	14.208(3)	28.0346(5)	28.375(2)	13.0370(2)	11.8601(5)
α (deg)	94.499(10)	90.000	90.000	105.997(1)	89.855(2)
β (deg)	100.101(17)	90.000	91.231(5)	97.766(1)	79.578(2)
γ (deg)	91.261(11)	90.000	90.000	99.529(1)	89.086(2)
V (Å^3)	856.5(3)	1600.85(5)	1664.5(2)	1042.61(4)	945.94(7)
Z	2	4	4	2	2
D_{calc} (g·cm^{-3})	1.584	1.892	2.018	1.718	1.941
μ (mm^{-1})	0.650	3.672	2.678	1.315	1.440
θ range (deg)	2.26−33.39	1.45−33.16	3.67−27.50	1.66−30.52	1.75−30.55
no. of rflns collected	26691	8627	1986	29522	35996
R_{int}	0.0583	0.0460	0.0749	0.0570	0.0263
no. of obsd rflns ($I > 2\sigma(I)$)	4822	1512	1876	4860	5457
no. of data/restraints/params	6435/250/304	1682/2/98	1986/158/173	6339/419/451	5771/0/294
GOF (on F^2)	1.051	1.232	1.175	1.021	1.049
R factors ($I > 2\sigma(I)$)	R1 = 0.0506	R1 = 0.0433	R1 = 0.0487	R1 = 0.0396	R1 = 0.0177
	wR2 = 0.0853	wR2 = 0.0968	wR2 = 0.0545	wR2 = 0.0610	wR2 = 0.0194
R factors (all data)	R1 = 0.0896	R1 = 0.0503	R1 = 0.1140	R1 = 0.0828	R1 = 0.0430
	wR2 = 0.1013	wR2 = 0.0990	wR2 = 0.1168	wR2 = 0.0921	wR2 = 0.0438
max peak/hole (e Å^{-3})	0.510/−0.456	0.935/−1.565	1.282/−1.912	0.752/−0.569	0.563/−0.408
CCDC no.	2088842	2088843	2088844	2088845	2088846

two components were integrated using SAINT and corrected for absorption using TWINABS, resulting in the following statistics.

For $CaL_2{\cdot}H_2O$: 9604 data (2479 unique) involve domain 1 only, mean I/σ 7.7; 9585 data (2482 unique) involve domain 2 only, mean I/σ 5.1; 17201 data (5002 unique) involve 2 domains, mean I/σ 6.1. The exact twin matrix identified by the integration program was found to be as follows: −0.99997, 0.00016, 0.00004; −0.00089, −1.00007, −0.00061; 0.90868, 0.21002, 1.00004.

For $BaL_2{\cdot}H_2O$: 2673 data (800 unique) involve domain 1 only, mean I/σ 4.4; 2611 data (770 unique) involve domain 2 only, mean I/σ 2.6; 14783 data (3885 unique) involve 2 domains, mean I/σ 3.2; 18 data (16 unique) involve 3 domains, mean I/σ 5.7. The exact twin matrix identified by the integration program was found to be as

https://doi.org/10.1021/acs.cgd.1c00683
Cryst. Growth Des. 2021, 21, 5421−5439

follows: 1.00000, −0.00002, 0.00002; −0.00007, −1.00000, 0.00004; −0.23943, −0.00027, −1.00000.

Both structures were solved using direct methods with only the nonoverlapping reflections of component 1. The structures were refined using the hklf 5 routine with all reflections of component 1 (including the overlapping reflections), resulting in BASF values of 0.3364(9) (Ca) and 0.293(3) (Ba). The R_{int} values given are for all reflections and are based on an agreement between observed single and composite intensities and those calculated from refined unique intensities and twin fractions. Water H atom positions were refined, and O−H and H···H distances were restrained to 0.84(2) and 1.36(2) Å, respectively, and further restrained on the basis of hydrogen-bonding considerations.

The two SO_3 groups in $CaL_2{\cdot}H_2O$ are disordered by a slight rotation. The disorder extends to the water molecule bridging between Ca ions. Both disordered SO_3 moieties were restrained to have similar geometries. U_{ij} components of ADPs for disordered atoms closer to each other than 2.0 Å were restrained to be similar. Disordered S atoms were constrained to have identical ADPs. Subject to these conditions, the occupancy ratio refined to 0.493(9)/0.507(9).

The pyrazole unit in $BaL_2{\cdot}H_2O$ is disordered by an approximate 2-fold rotation around the S1−C3 axis. U_{ij} components of ADPs for disordered atoms closer to each other than 2.0 Å were restrained to be similar. Subject to these conditions, the occupancy ratio refined to 0.511(10)/0.489(10). In the Rb, Cs, and Sr structures, the pyrazole unit is disordered (0.50/0.50) about a mirror plane bisecting the sulfonate group.

In $CuL_2(H_2O)_3{\cdot}2.3H_2O{\cdot}0.5C_3H_6O$, one water molecule (of O12) was refined as 3-fold disordered. One of the disordered moieties, O12B, is associated with an additional second water molecule, O13B. Water H atom positions were refined, and O−H and H···H distances were restrained to 0.84(2) and 1.36(2) Å, respectively. Some water H atom positions were further restrained on the basis of hydrogen-bonding considerations. An acetone molecule, located across an inversion center, was refined as 6-fold disordered (three independent moieties, pairs of molecules are symmetry equivalent by inversion). The exact orientations of acetone molecules are ill-defined, and the model is an approximation. C−O and C−C bond lengths and some angles (1,3-distances) were restrained to the expected target values. One molecule (of O14) was restrained to be close to planar. The occupancies of each one of the acetone moieties were set to be equal on the basis of H-bonding interactions. U_{ij} components of ADPs for disordered atoms closer to each other than 2.0 Å were restrained to be similar. Subject to these conditions, the occupancy rates refined to 0.488(3) (water of O12), 0.346(3) (waters of O12B and O13B), 0.1656(14) (water of O12C and acetone of O14C), 0.1782(15) (acetone of O14), and 0.1562(15) (acetone of O14B).

Crystallographic details are summarized in Table 1. Crystallographic data have been deposited with the Cambridge Crystallographic Data Center (CCDC 2088836 and 2088838−2088846). Copies of the data can be obtained free of charge at http://www.ccdc.cam.ac.uk/products/csd/request.

RESULTS AND DISCUSSION

Reactions of 3,5-dimethylpyrazole-4-sulfonic acid in aqueous solution with NH_3, Li_2CO_3, $Na_2CO_3{\cdot}H_2O$, K_2CO_3, Rb_2CO_3, Cs_2CO_3, MgO, $CaCO_3$, $SrCO_3$, $BaCO_3$, CuO, and CdO, respectively, provide the corresponding ammonium salt or metal−sulfonate coordination polymers and complexes, obtained as colorless or blue (in the case of Cu) crystals after water evaporation. All compounds are soluble in water, dimethyl sulfoxide, and ethylene glycol.

Description of the Crystal Structures. *HL·H₂O.* As expected for nitrogen-containing heterocycles bearing acidic groups, 3,5-dimethylpyrazole-4-sulfonic acid has a zwitterionic structure (Figure 1). As opposed to pyrazole-4-sulfonic acid,[71] which has a mirror plane bisecting the molecule, the 3,5-dimethylpyrazole-4-sulfonic acid molecule is located on a general position within the triclinic crystal lattice. The N−H hydrogen atoms of the HL zwitterion are involved in H bonding with one sulfonate O atom of an adjacent molecule as well as an H_2O molecule (Table 2), whereas in the anhydrous pyrazole-4-sulfonic acid they are both H-bonded to the two O atoms of an adjacent sulfonate moiety. Another difference between the two structures is that in pyrazole-4-sulfonic acid there are no aromatic interactions, whereas in HL the pyrazole units form pairs with a centroid···centroid distance of 3.893(2) Å and a plane···plane separation of 3.403(2) Å (the angle between pyrazole planes is 0°, crystallographically imposed). The centroid···centroid distance between adjacent pairs is 4.355(2) Å (with a plane···plane separation of 3.564(3) Å).

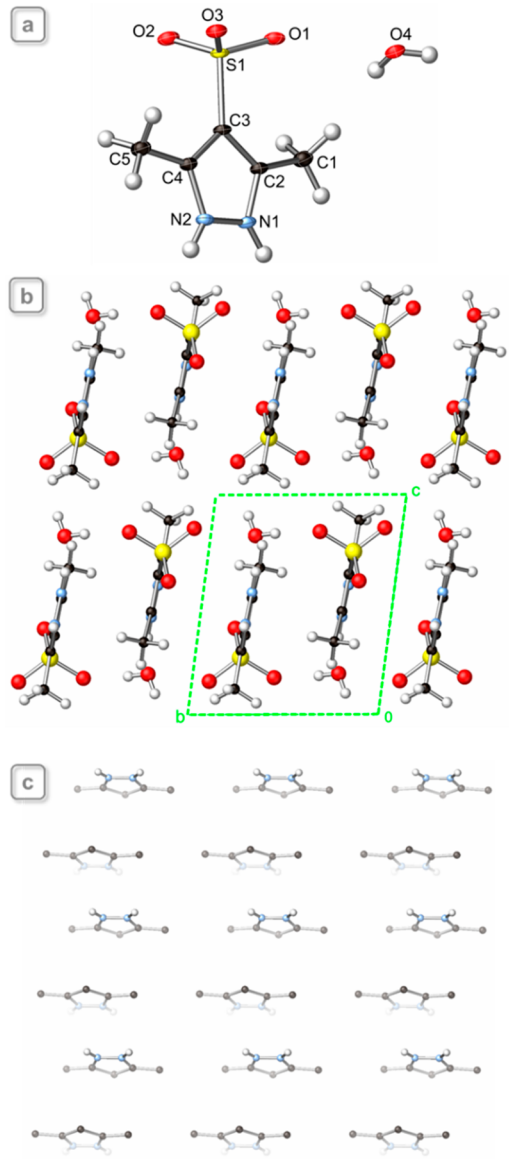

Figure 1. (a) Thermal ellipsoid plot (50% probability), (b) packing diagram, and (c) view perpendicular to the organic layer in $HL{\cdot}H_2O$, illustrating the aromatic interaction pattern.

LiL(H₂O). In the crystal lattice of $LiL(H_2O)$ (orthorhombic, *Aba*2), the Li^+ ion is 4-coordinate in a slightly distorted tetrahedral environment, by two O atoms from two different SO_3^- groups and two H_2O molecules (Figures 2 and 3 and Table 3). Within the inorganic layer (Figure 4), all Li^+ ions are

https://doi.org/10.1021/acs.cgd.1c00683
Cryst. Growth Des. 2021, 21, 5421−5439

Table 2. Summary of Hydrogen-Bonding Data for the Reported Compounds

Compound	D−H···A	D−H (Å)	H···A (Å)	D···A (Å)	D−H···A (deg)	symmetry operator for A
HL	O4−H4B···O2	0.79(2)	1.98(2)	2.755(2)	169(3)	$-x+1, -y+1$
	O4−H4A···O3	0.81(2)	2.04(2)	2.822(2)	162(3)	$x, y, z+1$
	N1−H1···O4	0.86	1.76	2.600(2)	163	$x-1, y, z$
	N2−H2···O1	0.86	1.82	2.669(2)	171	$x-1, y, z$
LiL	O4−H4a···O2	0.87(2)	1.90(2)	2.749(2)	165(2)	$-x+1, -y+1, z+1$
	O4−H4b···O2	0.84(2)	1.94(2)	2.772(2)	168(2)	$x, y, z+1$
	N2−H2···N1	0.86(2)	2.03(2)	2.887(3)	175(2)	$-x+1, -y+3/2, z+1/2$
NaL	O4−H4A···O1	0.97	1.90	2.826(1)	158	$x, -y+1/2, z+1/2$
	O4−H4B···O2	0.97	1.99	2.857(1)	147	
	N1−H1···N2	0.86	2.09	2.899(1)	158	$-x+1, y+1/2, -z+1/2$
RbL	N2−H2···N1	0.84	2.09	2.916	168	$-x+1/2, y+1/2, -z$
CsL	N1−H1···N2	0.86	2.10	2.930	163	$-x+1/2, y+1/2, -z$
CaL_2	O7A−H7B···O5A	0.82(2)	2.18(2)	2.894(10)	146(4)	$x-1, y, z$
	O7A−H7A···O5A	0.84(2)	1.81(4)	2.606(8)	156(8)	$-x+2, -y+2, -z+1$
	O7B−H7C···O5B	0.82(2)	2.19(6)	2.717(8)	122(6)	$-x+2, -y+2, -z+1$
	O7B−H7D···O7B	0.85(2)	2.17(3)	2.756(12)	126(4)	$-x+2, -y+2, -z+1$
	N1−H1···N4	0.88	2.11	2.928(3)	154	$-x+2, -y+1, -z$
	N3−H3···N2	0.88	2.06	2.910(3)	161	$-x+1, -y+1, -z$
SrL_2	N1−H1···N2	0.86	2.05	2.882	164	$-x+3/2, -y+3/2, -z+1$
BaL_2	O4−H4···O2	0.83(2)	2.22(3)	3.017(9)	161(3)	$x+1/2, y-1/2, z$
	N1−H1···N1	0.88	2.27	2.95(3)	134	$-x+1/2, -y+3/2, -z+1$
CuL_2	O7−H7A···O10	0.79(2)	1.98(2)	2.749(3)	164(3)	
	O7−H7B···O2	0.82(2)	2.05(2)	2.832(2)	158(3)	$-x+1, -y+2, -z+1$
	O8−H8A···O3	0.82(2)	2.10(2)	2.894(3)	165(3)	$-x, -y+2, -z+1$
	O8−H8B···O3	0.84(2)	2.09 (2)	2.930(2)	176(3)	$x, y-1, z$
	O9−H9A···O1	0.83(2)	1.87(2)	2.692(2)	174(3)	$x, y-1, z$
	O9−H9B···O4	0.82(2)	1.89(2)	2.698(2)	174(3)	$-x+1, -y+2, -z+2$
	O9−H9B···O6	0.82(2)	2.57(3)	2.958(2)	110(2)	$-x+1, -y+2, -z+2$
	O10−H10A···O1	0.83(2)	2.15(2)	2.950(3)	161(2)	$-x+1, -y+2, -z+1$
	O10−H10B···O2	0.82(2)	2.23(2)	3.034(3)	167(4)	$x, y-1, z$
	O12−H12B···O10	0.84(2)	2.20(2)	3.005(7)	163(6)	$-x, -y+1, -z+1$
	O12B−H12C···O3	0.87(2)	2.12(2)	2.965(7)	164(7)	$x, y-1, z$
	O12B−H12D···O13B	0.84(2)	1.95(5)	2.766(10)	163(14)	
	O13B−H13A···O4	0.85(2)	2.00(2)	2.759(7)	149(5)	$-x, -y+2, -z+2$
	O13B−H13B···O10	0.84(2)	2.20(2)	2.707(8)	119(2)	$-x, -y+1, -z+1$
	N2−H2···O5	0.88	2.06	2.776(2)	138	$-x, -y+2, -z+2$
	N5−H5···O12	0.88	2.00	2.851(6)	162	
	N5−H5···O12B	0.88	1.99	2.836(6)	162	
	N5−H5···O12C	0.88	2.13	2.866(15)	141	
CdL_2	O7−H7A···O4	0.77(2)	2.06(2)	2.7915(14)	160(2)	$x, y+1, z$
	O7−H7B···O4	0.78(2)	2.01(2)	2.7863(14)	175(2)	$-x+2, -y+1$
	O8−H8A···O10	0.81(2)	1.89(2)	2.6790(15)	166(2)	
	O8−H8B···O5	0.80(2)	1.94(2)	2.7316(14)	173(2)	$-x+2, -y+1$
	O9−H9A···O2	0.79(2)	2.05(2)	2.8394(14)	177(2)	$x, y-1, z$
	O9−H9B···O1	0.77(2)	2.14(2)	2.8969(14)	167(2)	$-x+1, -y+2$
	O10−H101···O11	0.79(2)	1.96(2)	2.7174(15)	159(2)	
	O10−H102···O2	0.78(2)	2.04(2)	2.8116(15)	172(2)	$-x+2, -y+2, -z+1$
	O11−H111···O3	0.81(2)	1.90(2)	2.6934(14)	166(2)	$-x+1, -y+2, -z+1$
	O11−H112···O1	0.79(2)	2.07(2)	2.8600(14)	177(2)	$x, y-1, z$
	N2−H2···O1	0.83(2)	2.11(2)	2.9138(15)	164(2)	
	N4−H4···O8	0.81(2)	2.45(2)	2.9648(15)	123(2)	
	N4−H4···O11	0.81(2)	2.23(2)	2.9969(15)	158(2)	$-x+2, -y+1, -z+1$

https://doi.org/10.1021/acs.cgd.1c00683
Cryst. Growth Des. 2021, 21, 5421−5439

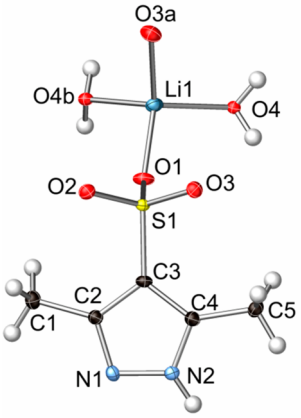

Figure 2. Thermal ellipsoid plot (50% probability) of LiL(H_2O), showing the coordination sphere around the Li ion. Symmetry codes: (a) $-x + 1, -y + 1, z$; (b) $-x + 1/2, y, z - 1/2$.

coplanar and are organized in infinite zigzag lines (with Li···Li distances of 3.218(6) Å and Li−O−Li angles of 110.2(2)°) by bridging H_2O molecules, which are also coplanar with the Li ions. The zigzag lines are interconnected by μ_2-sulfonate groups above and below the two-dimensional $[Li^+(H_2O)]_\infty$ layer, which also form H-bonds with the H_2O molecules (Table 2). Within the organic layer (Figure 5), the pyrazole moieties form a double layer. In each half of the organic layer, the pyrazole moieties are organized in a typical herringbone pattern, similar to the packing of the prototype molecule naphthalene.[72] The pyrazole units are parallel with centroid··· centroid distances of 5.520(1) Å and a plane···plane separation of 3.600(7) Å. The halves of the organic layer are interconnected by N−H···N hydrogen bonds between the pyrazole units (Table 2). This pattern is similar to that observed in Sr(4-SO_3-pzH)$_2$.[41]

NaL(H$_2$O). In the crystal lattice of NaL(H_2O) (monoclinic, $P2_1/c$), the Na^+ ion is 5-coordinate in a distorted-trigonal-bipyramidal environment, by three O atoms from three different SO_3^- groups and two H_2O molecules (Figures 3 and 6 and Table 3). The inorganic layer (Figure 4) is similar to that in LiL(H_2O), with Na^+ ions organized in infinite zigzag lines with Na···Na distances of 3.9812(7) Å and Na−O−Na angles of 115.08(3)° by bridging H_2O molecules. However, the Na^+ ions are not coplanar with each other or with the H_2O molecules. The inorganic layer in NaL(H_2O) can also be viewed as composed of halves; within each half, the Na^+ ions are interconnected by μ_3-sulfonate groups which also form H-bonds with the H_2O molecules (Table 2), whereas the halves are connected by μ_2-H_2O molecules between Na^+ ions. The structure of the organic layer is the same as that in LiL(H_2O), with parallel pyrazole planes at distances of 3.456(2) Å and centroid···centroid distances of 5.563(1) Å, organized in a herringbone pattern. The crystal structure of NaL(H_2O) has previously been determined at room temperature,[73] with R1 = 5.14% (vs 2.92% at 100 K reported here). Related complexes, wherein the pyrazole N−H hydrogen atom is replaced by either Cu^+ or Ag^+, have also been reported.[73,74]

RbL. In the anhydrous crystal lattice of RbL (monoclinic, $C2/m$), the Rb^+ ion is 9-coordinate by O atoms from six different SO_3^- groups (Figures 3 and 7 and Table 3). The inorganic layer (Figure 4) contains Rb^+ ions organized in two parallel planes, in which the Rb^+ ions are coplanar in a triangular grid pattern with Rb···Rb distances of 5.787(1), 5.901(1), and 5.901(1) Å, whereas interplanar distances between Rb^+ ions are 3.6007(2) and 3.6749(5) Å. The organic layer has the same structure as in LiL(H_2O), with parallel pyrazole planes at a distance of 3.431(7) Å (centroid··· centroid distance of 5.787(1) Å), organized in a herringbone pattern.

CsL. The crystal structure of CsL is isomorphous with that of RbL (Figures 3 and 8 and Table 3). The corresponding Rb···Rb distances are 5.963(1), 6.085(1), and 6.085(1) Å within one half-layer, and 3.7663(2) and 3.8295(6) Å between the two half-layers. Within the organic layer, a herringbone pattern is observed with parallel pyrazole planes at distances of 2.449(13) Å and centroid···centroid distances of 6.085(1) Å.

CaL$_2$(H$_2$O). In the crystal lattice of $CaL_2(H_2O)$ (triclinic, $P\bar{1}$), the Ca^{2+} ion is 6-coordinate in a slightly distorted octahedral environment, by five O atoms from five different SO_3^- groups and a H_2O molecule (Figures 3 and 9 and Table 3). Within the inorganic layer, infinite ribbons along the *a* axis are locked together by H-bonds between sulfonate groups and H_2O molecules (Figure 4 and Table 2). The ribbons consist of Ca ions arranged in a triangle strip by bridging μ_3-sulfonate groups (Ca···Ca distances: 5.447(1), 5.473(1), and 5.543(2) Å). Again, the structure of the organic layer is the same as that in LiL(H_2O), with parallel pyrazole planes at distances of 3.618(5) and 3.506(5) Å and centroid···centroid distances of 5.543(2) and 5.543(2) Å.

SrL$_2$(H$_2$O). In the crystal lattice of $SrL_2(H_2O)$ (orthorhombic, *Cmcm*), the Sr^{2+} ion is 8-coordinate in a distorted bicapped trigonal prismatic environment, by six O atoms from six different SO_3^- groups forming the distorted trigonal prism and two H_2O molecule caps (Figures 3 and 10 and Table 3). The inorganic layer (Figure 4) is similar to that in the Li analogue in that all Sr^{2+} ions are coplanar and to the Na and Ca analogues in that the sulfonate groups are μ_3-bridging (Sr···Sr distances: 5.970(1), 5.349(1) Å). The structure of the organic layer is the same as in LiL(H_2O), with parallel pyrazole planes at distances of 3.385(11) Å and centroid···centroid distances of 5.349(1) Å. Hydrogen-bonding data are given in Table 2.

BaL$_2$(H$_2$O). The coordination geometry of the 8-coordinate Ba^{2+} ion in the crystal lattice of $BaL_2(H_2O)$ (monoclinic, $C2/c$) is very similar to that of the Sr analogue, with the exception that the triangular faces of the bicapped trigonal prism formed by the six sulfonate O atoms are not perfectly eclipsed as in the Sr analogue (Figures 3 and 11 and Table 3). This difference can also be seen in Figure 4, which shows the structure of the inorganic layer (Ba···Ba distances: 5.2805(4) and 6.1510(3) Å). Once again, the structure of the organic layer is the same as in LiL·H_2O, with parallel pyrazole planes at distances of 3.40(4) Å and centroid···centroid distances of 5.2805(4) Å. The corresponding hydrogen-bonding data are given in Table 2.

CuL$_2$(H$_2$O)$_3$·2.3H$_2$O·0.5C$_3$H$_6$O. In the triclinic ($P\bar{1}$) crystal lattice of the copper(II) complex, the Cu^{2+} ion is 6-coordinate in a distorted-octahedral environment, by two pyrazole N atoms (in a *cis* geometry) and two H_2O molecules in the equatorial plane, and a sulfonate O atom and a H_2O molecule in the axial positions (Figure 12 and Table 3). In contrast to all other metal complex analogues studied so far, there are no distinct inorganic and organic layers in the Cu^{2+} complex of L. Instead, layers of the metal complex separated by H_2O/acetone layers are observed (Figures 3 and 4). Within these layers, the shortest Cu···Cu distance is 7.2128(5) Å, whereas the shortest Cu···Cu distance between the layers is 8.0675(5) Å. Several

https://doi.org/10.1021/acs.cgd.1c00683
Cryst. Growth Des. 2021, 21, 5421−5439

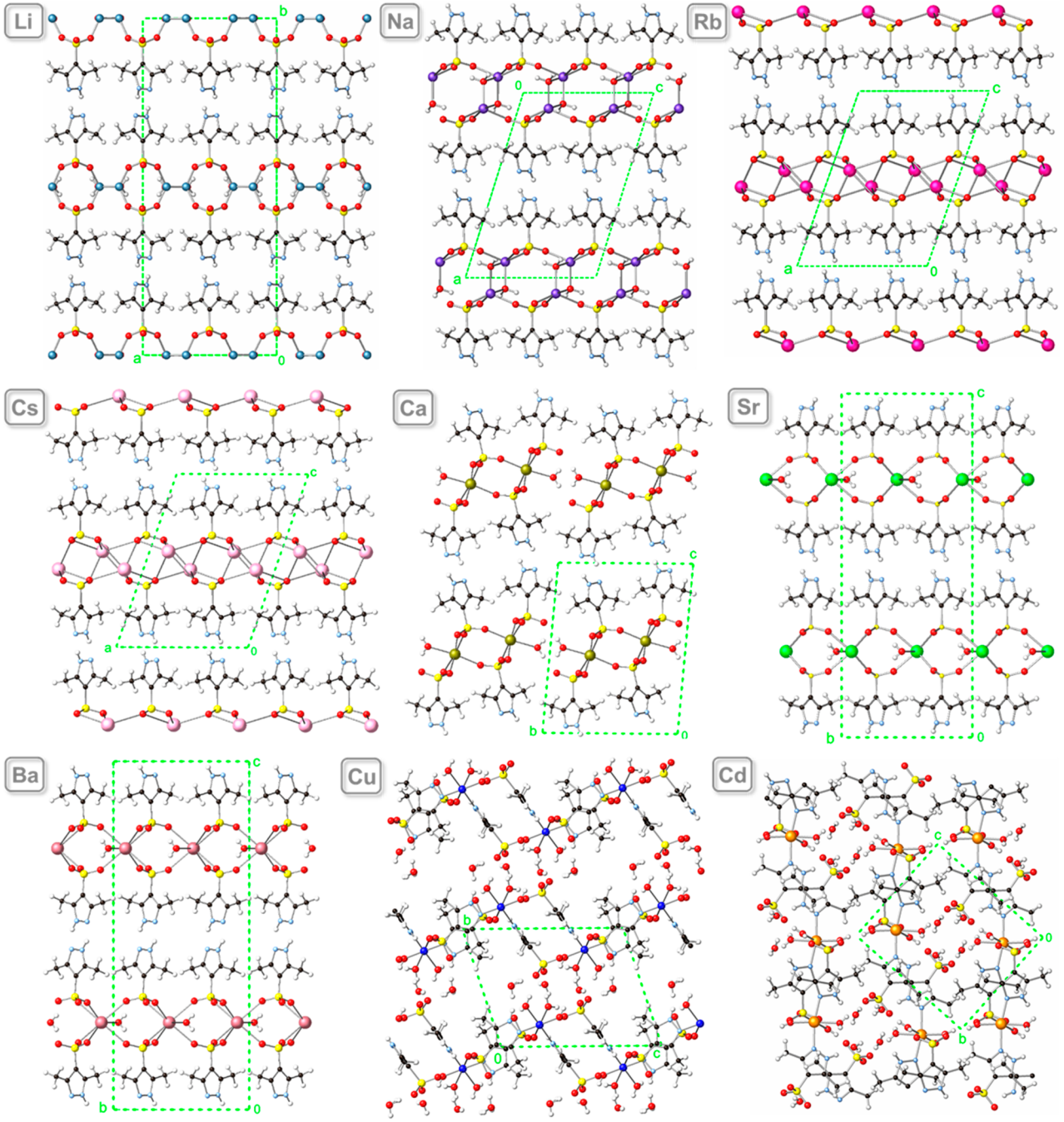

Figure 3. Packing diagrams of the different coordination compounds of L showing alternating inorganic−organic layers. In the case of CuL_2, which lacks distinct inorganic−organic layers, layers of the metal complex separated by H_2O/acetone layers are observed instead (only one position of the disordered H_2O molecule is shown, and the disordered acetone molecule is omitted for clarity).

hydrogen-bonding interactions are present between the H_2O molecules and the pyrazole and sulfonate moieties (Table 2). The two individual pyrazole moieties are involved in two different types of aromatic interactions (Figure 5). In one, parallel pyrazole units form isolated stacks at distances of 3.441(3) Å (centroid···centroid distance of 4.473(2) Å). In the other, parallel pyrazole units stack to form infinite offset columns at distances of 3.445(5) Å (centroid···centroid: 4.664(2) Å) and 3.650(5) Å (centroid···centroid: 4.852(2) Å).

$CdL_2(H_2O)_3·2H_2O$. In the crystal lattice of $CdL_2(H_2O)_3·2H_2O$ (triclinic, $P\bar{1}$), the Cd^{2+} ion is 6-coordinate in a distorted-octahedral environment, by two pyrazole N atoms (in a *trans* geometry), three H_2O molecules, and a sulfonate O atom (Figure 13 and Table 3). Unlike the Cu complex, the Cd complex does display distinct inorganic and organic layers (Figure 3), although they are undulating as opposed to the flat layers in the corresponding alkali and alkaline-earth derivatives. Within the inorganic layer (Figure 4), Cd^{2+} ions are found in linear arrangements with Cd···Cd distances of 7.9624(3) Å, which are coupled into strips by H-bonds between adjacent sulfonate groups and H_2O molecules (Cd···Cd separation: 7.2046(5) Å) (Table 2). The strips are further connected into undulating layers by noncoordinating sulfonate groups and H_2O molecules (Cd···Cd separation: 9.4065(5) Å). Within the

https://doi.org/10.1021/acs.cgd.1c00683
Cryst. Growth Des. 2021, 21, 5421−5439

Table 3. Selected Bond Lengths (Å) of the Reported Coordination Compounds

compound							symmetry operators
LiL	Li1−O1	1.906(6)	Li1−O4	1.961(7)	S1−O1	1.453(2)	(a) $-x+1, -y+1, z$; (b) $-x+1/2, y, z-1/2$
	Li1−O3a	1.916(6)	Li1−O4b	1.963(6)	S1−O2	1.466(2)	
					S1−O3	1.453(2)	
NaL	Na1−O1	2.3280(7)	Na1−O3b	2.3315(7)	S1−O1	1.4674(6)	(a) $x, y-1, z$; (b) $x, -y+1/2, z+1/2$; (c) $-x, y-1/2, -z+1/2$
	Na1−O2a	2.3168(7)	Na1−O4	2.3954(7)	S1−O2	1.4566(6)	
			Na1−O4c	2.3228(8)	S1−O3	1.4547(7)	
RbL	Rb1−O1	3.096(1)	Rb1−O2d	3.0411(4)	Rb1−O1g	3.096(1)	(a) $-x+1/2, -y+5/2, -z+1$; (b) $-x+1/2, y-1/2$; (c) $-x+1, -y+2, -z+1$; (d) $x-1/2, y-1/2, z$; (e) $x-1/2, y+1/2, z$; (f) $x-1/2, -y+5/2, z$; (g) $x, -y+2, z$
	Rb1−O1a	2.923(1)	Rb1−O2e	3.0411(4)	S1−O1	1.459(1)	
	Rb1−O1b	2.923(1)	Rb1−O1d	3.081(1)	S1−O1g	1.459(1)	
	Rb1−O2c	2.977(1)	Rb1−O1f	3.081(1)	S1−O2	1.461(1)	
CsL	Cs1−O1	3.192(1)	Cs1−O2d	3.1417(6)	Cs1−O2g	3.212(2)	(a) $-x+1/2, -y+1/2$; (b) $-x+1/2, y-1/2, -z+1$; (c) $x-1/2, y-1/2, z$; (d) $x-1/2, y+1/2, z$; (e) $x-1/2, -y+1/2, z$; (f) $x, -y, z$; (g) $-x+1, -y, -z$
	Cs1−O1a	3.119(1)	Cs1−O1c	3.173(1)	S1−O1	1.461(2)	
	Cs1−O1b	3.119(1)	Cs1−O1e	3.173(1)	S1−O1f	1.461(2)	
	Cs1−O2c	3.1417(6)	Cs1−O1f	3.192(1)	S1−O2	1.462(2)	
CaL_2	Ca1−O1Ba	2.284(8)	Ca1−O7B	2.337(5)	S1B−O1B	1.45(1)	(a) $-x+2, -y+1, -z+1$; (b) $-x+1, -y+1, -z+1$; (c) $x-1, y, z$
	Ca1−O3Bb	2.297(5)	Ca1−O6Bc	2.35(1)	S1B−O3B	1.45(1)	
	Ca1−O2A	2.298(6)	Ca1−O7A	2.350(5)	S2A−O4A	1.44(1)	
	Ca1−O6Ac	2.31(1)	Ca1−O1Aa	2.356(7)	S2A−O5A	1.46(1)	
	Ca1−O3Ab	2.318(5)	S1A−O3A	1.44(1)	S2A−O6A	1.46(1)	
	Ca1−O4B	2.320(5)	S1A−O1A	1.44(1)	S2B−O5B	1.43(1)	
	Ca1−O4A	2.323(6)	S1A−O2A	1.46(1)	S2B−O6	1.45(1)	
	Ca1−O2B	2.330(5)	S1B−O2B	1.44(1)	S2B−O4B	1.46(1)	
SrL_2	Sr1−O1a	2.504(3)	Sr1−O2d	2.542(2)	S1−O1	1.452(3)	(a) $-x+2, y, -z+3/2$; (b) $-x+5/2, y+1/2, -z+3/2$; (c) $x-1/2, y+1/2, z$; (d) $x-1/2, y+1/2, -z+3/2$; (e) $-x+5/2, y+1/2, z$; (f) $x+1, y, z$; (g) $-x+2, y, z$
	Sr1−O1	2.504(3)	Sr1−O2e	2.542(2)	S1−O2	1.445(2)	
	Sr1−O2b	2.542(2)	Sr1−O3	2.946(2)	S1−O2g	1.445(2)	
	Sr1−O2c	2.542(2)	Sr1−O3f	2.946(2)			
BaL_2	Ba1−O1a	2.700(6)	Ba1−O3d	2.736(6)	S1−O1	1.448(6)	(a) $-x+1/2, y-1/2, -z+1/2$; (b) $x-1/2, y-1/2, z$; (c) $-x, y, -z+1/2$; (d) $-x+1, y, -z+1/2$; (e) $x-1, y, z$
	Ba1−O1b	2.700(6)	Ba1−O3e	2.736(6)	S1−O2	1.463(6)	
	Ba1−O2c	2.731(6)	Ba1−O4	2.988(3)	S1−O3	1.443(6)	
	Ba1−O2	2.731(6)	Ba1−O4e	2.988(3)			
CuL_2	Cu1−O6a	2.390(2)	Cu1−N1	2.012(2)	S1−O3	1.464(2)	(a) $-x+1, -y+2, -z+2$
	Cu1−O7	1.992(2)	Cu1−N4	1.994 (2)	S2−O4	1.464(2)	
	Cu1−O8	2.319(2)	S1−O1	1.460(2)	S2−O5	1.446(2)	
	Cu1−O9	2.002(2)	S1−O2	1.456(2)	S2−O6	1.463(2)	
CdL_2	Cd1−O6a	2.267(1)	Cd1−N1	2.306(1)	S1−O3	1.454(1)	(a) $-x+1, -y+1, -z+2$
	Cd1−O7	2.304(1)	Cd1−N3	2.329(1)	S2−O4	1.463(1)	
	Cd1−O8	2.269(1)	S1−O1	1.463(1)	S2−O5	1.449(1)	
	Cd1−O9	2.330(1)	S1−O2	1.469 (1)	S2−O6	1.471(1)	

organic layer (Figure 5), the two individual pyrazole moieties each form parallel pairs with plane−plane distances of 3.540(2) and 3.684(1) Å, respectively (centroid···centroid distances of 4.360(1) and 3.725(1) Å). The stacked pairs form further interactions with plane−plane distances of 3.904(3) and 3.430(3) Å, respectively (centroid···centroid distances of 5.343(1) and 5.273(1) Å). In contrast to the alkali and alkaline-earth derivatives, where the pyrazole N−H hydrogen atoms are involved in H-bonding with other pyrazole moieties, here the N−H hydrogen atoms form H-bonds with lattice H_2O molecules (Table 2).

Effect of the Methyl Substituents on the Molecular and Supramolecular Structure of Pyrazole-4-sulfonate Networks. The addition of two methyl groups to the pyrazole moiety of the pyrazole-4-sulfonate ligand leads to major changes in the crystal structure of the corresponding coordination compounds (Table 4). Due to the steric hindrance introduced by the methyl groups, the pyrazole units in 3,5-dimethylpyrazole-4-sulfonate networks cannot engage in edge-to-face interactions, as in the case of the parent pyrazole-4-sulfonate networks.

No aromatic interactions are present in the crystal structure of pyrazole-4-sulfonic acid, because of the dominating, chelatelike pair of H-bonds formed between the two pyrazole N−H groups of the ligand and two O atoms of an SO_3 group from an adjacent molecule. In the crystal structure of 3,5-dimethylpyrazole-4-sulfonic acid, only one pyrazole N−H group forms a hydrogen bond to a sulfonate group, whereas the other group forms a hydrogen bond to an H_2O molecule. The different H-bond pattern in the latter allows for weak $\pi-\pi$

https://doi.org/10.1021/acs.cgd.1c00683
Cryst. Growth Des. 2021, 21, 5421−5439

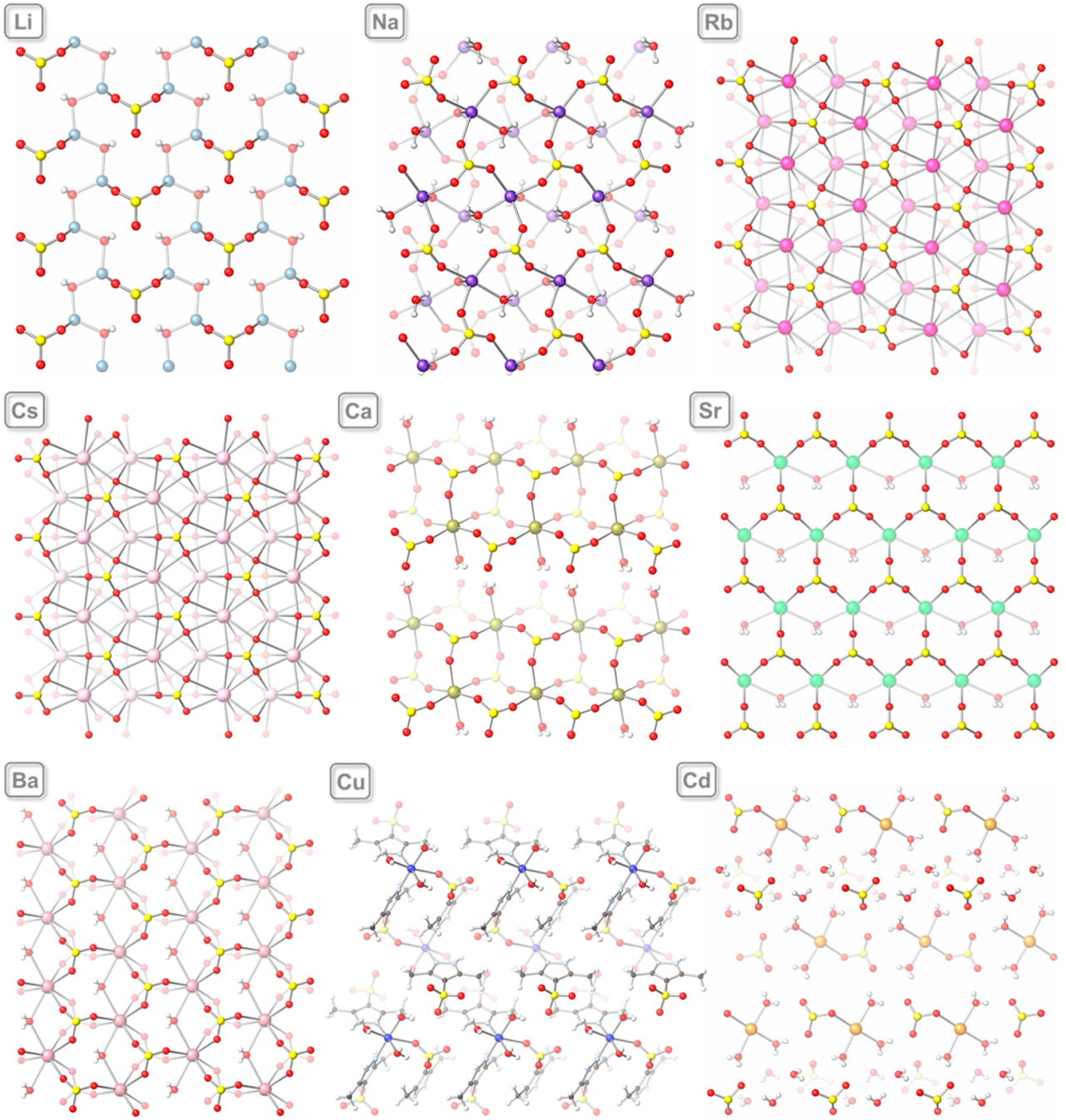

Figure 4. View perpendicular to the inorganic layer in the different coordination polymers and discrete metal complexes of L. In the case of CuL_2, which lacks distinct inorganic−organic layers, the metal complex layer is shown instead.

stacking interactions. The plane···plane separation of 3.40 Å and centroid···centroid distance of 3.89 Å are the shortest observed in the 3,5-dimethylpyrazole-4-sulfonate series of compounds.

Only stacking arrangements have been observed in the metal complexes of 3,5-dimethylpyrazole-4-sulfonate studied so far, with pyrazole centroid···centroid distances of 5.28−5.96 Å (plane···plane separations of 3.39−3.62 Å) in the case of the alkali and alkaline-earth coordination compounds. These values are significantly larger than the corresponding values observed with pyrazole-4-sulfonate, which have centroid···centroid distances as short as 3.49 Å and plane···plane separations as close as 3.18 Å. This discrepancy is due to the presence of the methyl substituents, which do not allow for efficient $\pi-\pi$ stacking interactions but form C−H···π interactions instead. In most pyrazole-4-sulfonate coordination compounds studied (except Mg, Ca, Cu, and Cd), edge-to-face interactions are also present in addition to the $\pi-\pi$ stacking interactions; in the case of the Rb and Sr compounds, only edge-to-face interactions are observed.[41]

Another major difference caused by the methyl substituents is that, while the pyrazole N−H groups form H-bonds with sulfonate O atoms in the case of pyrazole-4-sulfonate, they form H-bonds with pyrazole N atoms in the case of 3,5-dimethylpyrazole-4-sulfonate. The difference in the aromatic interaction and H-bonding patterns is translated into a drastic

https://doi.org/10.1021/acs.cgd.1c00683
Cryst. Growth Des. 2021, 21, 5421−5439

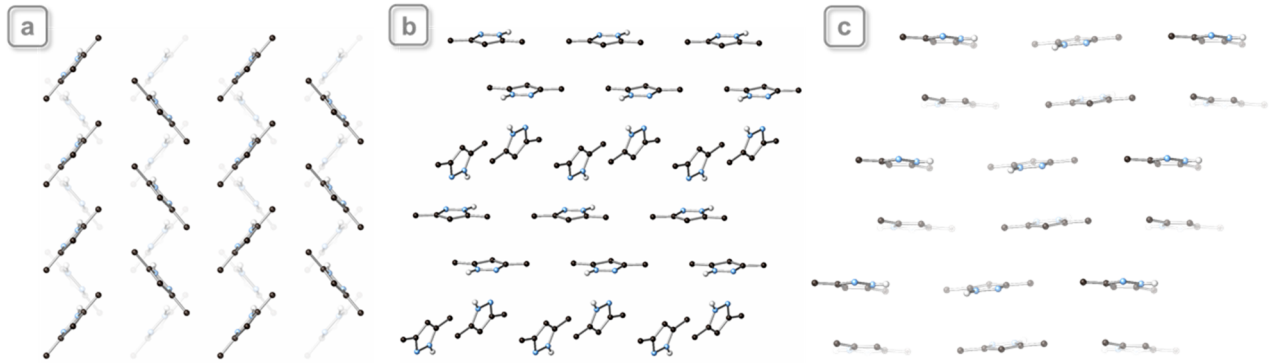

Figure 5. View perpendicular to the organic layer in the different coordination compounds of L, illustrating the aromatic interaction pattern. The same herringbone pattern (a) is observed in the Li, Na, Rb, Cs, Ca, Sr and Ba coordination polymers, whereas CuL_2 (b) and CdL_2 (c) show distinct patterns of sandwiches and offset stacked columns.

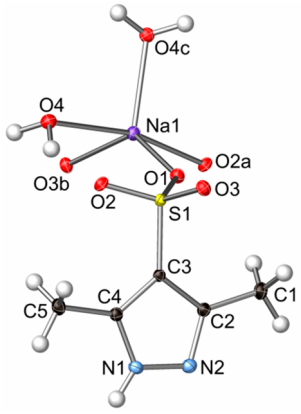

Figure 6. Thermal ellipsoid plot (50% probability) of $NaL(H_2O)$, showing the coordination sphere around the Na ion. Symmetry codes: (a) $x, y - 1, z$; (b) $x, -y + 1/2, z + 1/2$; (c) $-x, y - 1/2, -z + 1/2$.

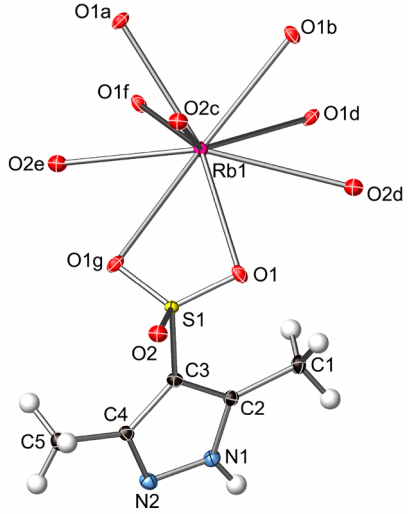

Figure 7. Thermal ellipsoid plot (50% probability) of RbL, showing the coordination sphere around the Rb ion. The pyrazole unit is disordered (50/50) about a mirror plane bisecting the sulfonate group (only one is shown). Symmetry codes: (a) $-x + 1/2, -y + 5/2, -z + 1$; (b) $-x + 1/2, y - 1/2$; (c) $-x + 1, -y + 2, -z + 1$; (d) $x - 1/2, y - 1/2, z$; (e) $x - 1/2, y + 1/2, z$; (f) $x - 1/2, -y + 5/2, z$; (g) $x, -y + 2, z$.

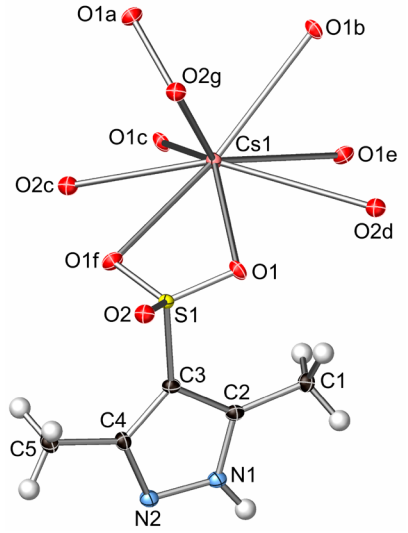

Figure 8. Thermal ellipsoid plot (50% probability) of CsL, showing the coordination sphere around the Cs ion. The pyrazole unit is disordered (50/50) about a mirror plane bisecting the sulfonate group (only one is shown). Symmetry codes: (a) $-x + 1/2, y - 1/2, -z + 1$; (b) $-x + 1/2, -y + 1/2, -z + 1$; (c) $x - 1/2, y - 1/2, z$; (d) $x - 1/2, y, z$; (e) $x - 1/2, -y + 1/2, z$; (f) $x, -y, z$; (g) $-x + 1, y, -z + 1$.

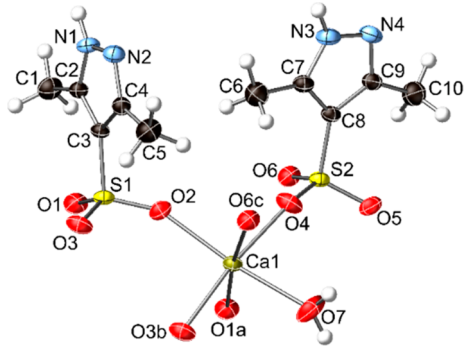

Figure 9. Thermal ellipsoid plot (50% probability) of $CaL_2(H_2O)$, showing the coordination sphere around the Ca ion. Only one of the two disordered sulfonate moieties and H_2O molecule is shown. Symmetry codes: (a) $-x + 2, -y + 1, -z + 1$; (b) $-x + 1, -y + 1, -z + 1$; (c) $x - 1, y, z$.

difference in the 3D structure of the compounds. Thus, the organic layer of the 3,5-dimethylpyrazole-4-sulfonate coordi-

https://doi.org/10.1021/acs.cgd.1c00683
Cryst. Growth Des. 2021, 21, 5421−5439

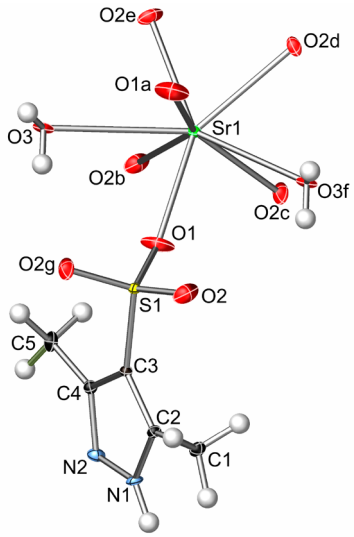

Figure 10. Thermal ellipsoid plot (50% probability) of $SrL_2(H_2O)$, showing the coordination sphere around the Sr ion. The pyrazole unit is disordered (50/50) about a mirror plane bisecting the sulfonate group (only one is shown). Symmetry codes: (a) $-x + 2, y, -z + 3/2$; (b) $-x + 5/2, y + 1/2, -z + 3/2$; (c) $x - 1/2, y + 1/2, z$; (d) $x - 1/2, y + 1/2, -z + 3/2$; (e) $-x + 5/2, y + 1/2, z$; (f) $x + 1, y, z$; (g) $-x + 2, y, z$.

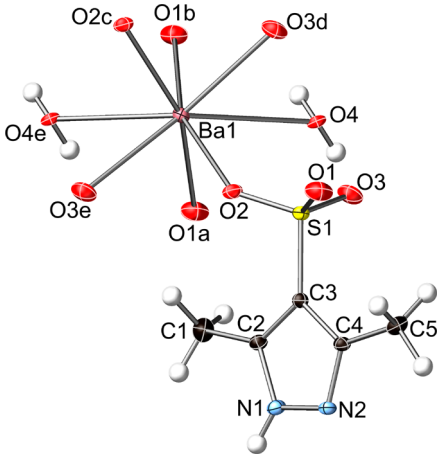

Figure 11. Thermal ellipsoid plot (50% probability) of $BaL_2(H_2O)$, showing the coordination sphere around the Ba ion. Only one of the two disordered pyrazole moieties is shown. Symmetry codes: (a) $-x + 1/2, y - 1/2, -z + 1/2$; (b) $x - 1/2, y - 1/2, z$; (c) $-x, y, -z + 1/2$; (d) $-x + 1, y, -z + 1/2$; (e) $x - 1, y, z$.

nation polymers contains two pyrazole layers hydrogen-bonded to each other, whereas that of the pyrazole-4-sulfonate compounds contains only a single layer of pyrazoles (with the exception of the Sr coordination polymer, which is similar to the 3,5-dimethylpyrazole-4-sulfonate derivative). The corresponding distances between the centers of adjacent inorganic layers are 13.86−15.08 and 6.79−9.96 Å, respectively (except for the Sr derivative in the latter case, where the distance is 14.17 Å). Exceptions to the trend described above are the Cu and Cd complexes of 3,5-dimethylpyrazole-4-sulfonate, which either do not form distinct inorganic−organic layers (Cu) or form a single layer of pyrazoles within the organic layer (inorganic layer center···center separation: 6.8 Å). In these last two complexes the pyrazole N−H groups form H-bonds with H_2O molecules, instead of sulfonate or pyrazole moieties.

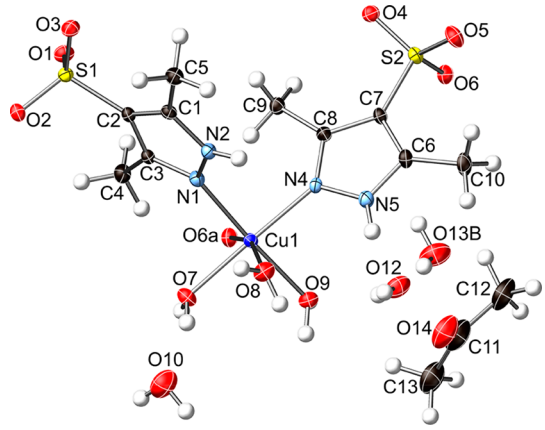

Figure 12. Thermal ellipsoid plot (50% probability) of $CuL_2(H_2O)_3 \cdot 2.3H_2O \cdot 0.5C_3H_6O$, showing the coordination sphere around the Cu ion. Only one of the disordered water and acetone molecules is shown. Symmetry code: (a) $-x + 1, -y + 2, -z + 2$.

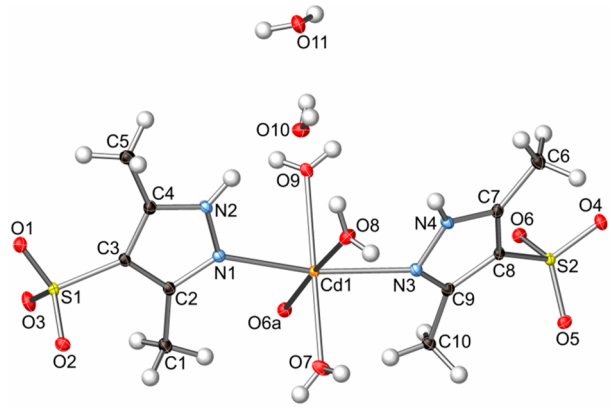

Figure 13. Thermal ellipsoid plot (50% probability) of $CdL_2(H_2O)_3 \cdot 2H_2O$, showing the coordination sphere around the Cd ion. Symmetry code: (a) $-x + 1, -y + 1, -z + 2$.

The effect of the methyl substituents extends from the organic layer to the inorganic layer. Thus, a reduction in the coordination number is observed on going from pyrazole-4-sulfonates to the corresponding dimethyl-substituted analogues in the case of Na (6 → 5), Ca (7 → 6), and Ba (10 → 8), while the coordination number increases in the case of Rb (8 → 9) and stays constant in the case of Cs (9), Sr (8), Cu (6), and Cd (6). The number of metal-coordinated H_2O molecules decreases in the case of Ca (3 → 1), and it increases in the case of Sr (0 → 2), Ba (1 → 2), Cu (2 → 3), and Cd (2 → 3), whereas the Rb and Cs analogues are anhydrous as the parent compounds. In the case of Na, two different forms of the pyrazole-4-sulfonate complexes are known, $NaL(H_2O)_2$ (with four coordinated H_2O molecules)[71] and $NaL(H_2O)$ (with two coordinated H_2O molecules),[42] whereas with the corresponding dimethyl derivative only one form is known (with two coordinated H_2O molecules). The sulfonate coordination modes also change on going from the parent compound to the dimethyl analogue (Scheme 1): from μ-κ^1:κ^1 (or μ_4-κ^2:κ^1:κ^1) to μ_3-κ^1:κ^1:κ^1 for Na, from μ_4-κ^2:κ^2:κ^2 to μ_6-κ^3:κ^3:κ^3 for Rb, from μ_5-κ^3:κ^2:κ^2 to μ_6-κ^3:κ^3:κ^3 for Rb, from κ^1 to μ-κ^1:κ^1 and μ_3-κ^1:κ^1:κ^1 for Ca, from μ_4-κ^2:κ^2:κ^1 to μ_3-κ^1:κ^1:κ^1 for Sr, from μ_4-κ^2:κ^2:κ^1 and μ-κ^2:κ^1 to μ_3-κ^1:κ^1:κ^1 for Ba, and from two κ^1 modes to one κ^1 and one noncoordinating mode for Cd (κ^1 in both Cu compounds).

https://doi.org/10.1021/acs.cgd.1c00683
Cryst. Growth Des. 2021, 21, 5421−5439

Table 4. Ionic Radii and Structural Parameters of 3,5-Dimethylpyrazole-4-sulfonate Coordination Compounds

cation	ionic radius[a] (Å)	metal coordination no.	no. of coordinated H_2O molecules	sulfonate coordination mode	aromatic interaction pattern	inorganic layer separation (Å)	metal−organic network dimensionality
Li^+	0.59	4	2	μ_2-κ^1:κ^1	herringbone	14.18	2D
Na^+	1.00	5	2	μ_3-κ^1:κ^1:κ^1	herringbone	15.08	2D
Rb^+	1.63	9	0	μ_6-κ^3:κ^3:κ^3	herringbone	13.83	2D
Cs^+	1.78	9	0	μ_6-κ^3:κ^3:κ^3	herringbone	13.96	2D
Ca^{2+}	1.00	6	1	μ_3-κ^1:κ^1:κ^1 and μ_2-κ^1:κ^1	herringbone	14.16	1D
Sr^{2+}	1.26	8	2	μ_3-κ^1:κ^1:κ^1	herringbone	14.02	2D
Ba^{2+}	1.42	8	2	μ_3-κ^1:κ^1:κ^1	herringbone	14.19	2D
Cu^{2+}	0.73	6	3	κ^1	sandwich and stacked columns		0D (dimers)
Cd^{2+}	0.65	6	3	κ^1	stacked columns	6.8	0D (dimers)

[a]Effective ionic radii correspond to the observed coordination numbers.[75]

Scheme 1. Coordination Modes of the Sulfonate Group Observed in This Work

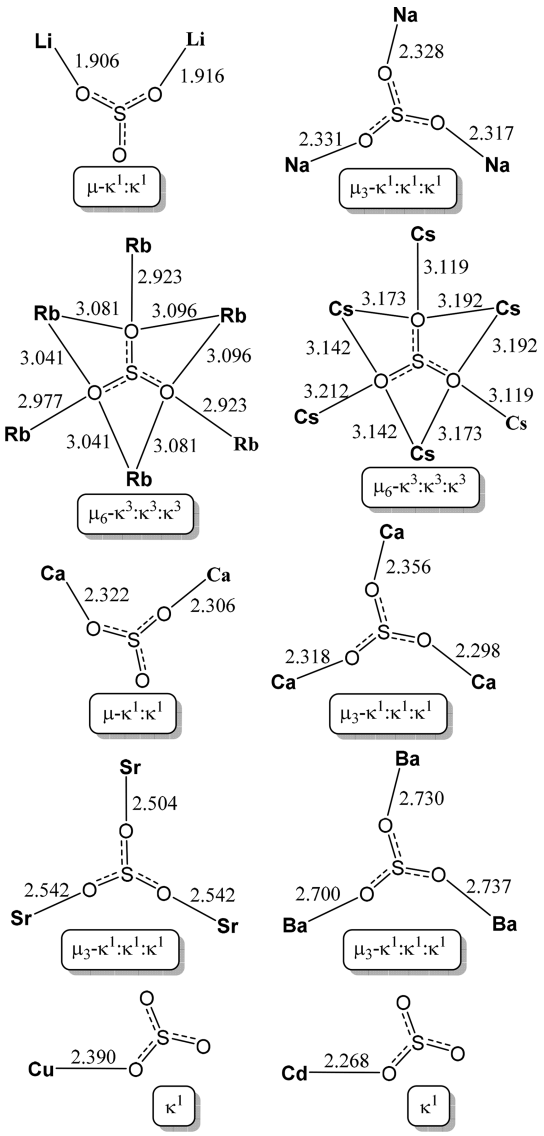

The crystal structures of the 3,5-dimethylpyrazole-4-sulfonate derivatives show that the alkali- and alkaline-earth-metal ions prefer coordination with the sulfonate groups, thus leaving the pyrazole moieties available for coordination to the copper metal surface when they are used as corrosion inhibitors. It is known that azoles, including pyrazole, can bind to and form films on metallic copper surfaces. Moreover, the crystal structures of the copper and cadmium derivatives confirm that the transition metal does bind to the pyrazole N atom. It is likely that, once the pyrazole moieties of the anticorrosion agents studied here are anchored onto the metallic copper surface, their sulfonate groups coordinate to the alkali- or alkaline-earth-metal ions present in solution and initiate the formation of the protecting films.

Topological Analysis. To get further insight into the metal−organic and hydrogen-bonded networks in the reported compounds, we performed their topological analysis and classification using the ToposPro software[76,77] and following a concept of the simplified underlying net.[78] For the analysis of metal−organic networks, the underlying nets were generated by omitting the terminal ligands, reducing all the bridging ligands to the corresponding centroids, and preserving their connectivity (M···M contacts were not considered). The obtained simplified nets were then classified from a topological viewpoint.

In the analysis of H-bonded networks, the molecular units were contracted to their centroids, maintaining connectivity via H-bonds. Following the default parameters in ToposPro for the analysis of H-bonds, D−H···A hydrogen bonds were considered[79] with H···A < 2.50 Å, D···A < 3.50 Å, and ∠(D−H···A) > 120°; D and A stand for donor and acceptor atoms.

HL·H$_2$O. An underlying network in HL·H_2O is assembled from the 5-connected HL molecular nodes and 3-connected H_2O nodes (Figure 14). This network can be classified as a binodal 3,5-connected bilayer with the **3,5L2** topology. It is

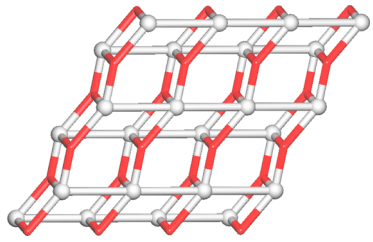

Figure 14. Topological representation of the 2D H-bonded network in HL·H_2O displaying a binodal 3,5-connected underlying bilayer with the **3,5L2** topology. View along the *b* axis (slightly rotated). Color codes: centroids of 5-connected HL nodes, gray spheres; centroids of 3-connected H_2O linkers, red.

https://doi.org/10.1021/acs.cgd.1c00683
Cryst. Growth Des. 2021, 21, 5421−5439

described by the point symbol $(4^2.6^7.8)(4^2.6)$ wherein the $(4^2.6^7.8)$ and $(4^2.6)$ indices correspond to the H_2O and HL nodes, respectively.

LiL(H_2O). An underlying 2D metal−organic network in this coordination polymer is assembled from the 3-connected Li nodes and 2-connected μ-L and μ-H_2O linkers (Figure 15). A topological analysis discloses a uninodal 3-connected decorated layer with the **hcb** (Shubnikov hexagonal plane net/(6,3)) topology and the point symbol (6^3).

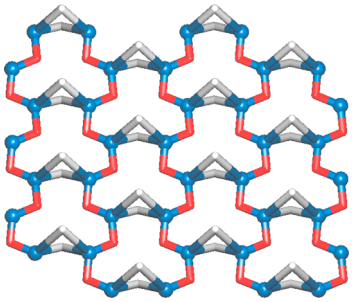

Figure 15. Topological representation of the 2D metal−organic network in LiL(H_2O) displaying a uninodal 3-connected underlying layer with the **hcb** topology. View along the *b* axis (slightly rotated). Color codes: 3-connected Li nodes, blue spheres; centroids of 2-connected μ-L linkers, gray, μ-H_2O linkers, red. The 2-connected μ-H_2O linkers were not considered for the topological classification (including the calculation of the point symbol).

NaL(H_2O). In contrast to LiL(H_2O), the structure of NaL(H_2O) is more complex, forming a bilayer 2D metal−organic network. An underlying bilayer in this compound is built from the 5-connected Na nodes, 3-connected μ_3-L nodes, and 2-connected μ-H_2O linkers (Figure 16a). The resulting

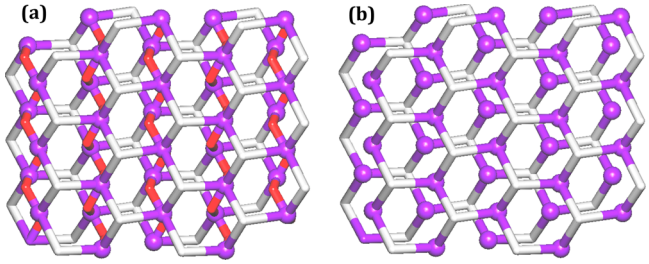

Figure 16. Topological representation of the 2D metal−organic network in NaL(H_2O). (a) Binodal 3,5-connected underlying bilayer with the unique topology defined by the point symbol $(4.6^2)(4^3.6^7)$. (b) Further simplified net obtained after omitting the μ-H_2O linkers, showing two uninodal 3-connected layers with the **hcb** topology. View along the *a* axis (slightly rotated). Color codes: Na nodes, purple spheres; centroids of 3-connected μ_3-L nodes, gray; centroids of 2-connected μ-H_2O linkers, red. The 2-connected μ-L linkers were not considered for the topological classification (including the calculation of the point symbol).

network can be classified as a binodal 3,5-connected net with the unique topology described by the point symbol (4.6^2)-$(4^3.6^7)$. The (4.6^2) and $(4^3.6^7)$ notations concern the μ_3-L and Na nodes, respectively. Further simplification of this bilayer by omitting the μ-H_2O linkers results in the formation of two uninodal 3-connected layers with an **hcb** topology (Figure 16b), which is similar to that of LiL(H_2O).

RbL and CsL. These 2D coordination polymers are topologically similar; the analysis of the metal−organic network in RbL is described. An underlying network is composed of the 6-connected Rb and μ_6-L nodes (Figure 17),

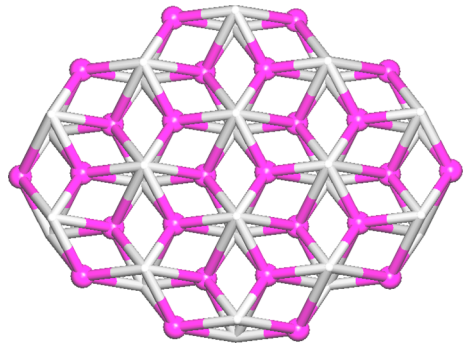

Figure 17. Topological representation of the 2D metal−organic network in RbL displaying a binodal 6,6-connected underlying bilayer with the **6,6L1** topology. View along the *c* axis (slightly rotated). Color codes: 6-connected Rb nodes, magenta balls; centroids of 6-connected μ_6-L nodes, gray.

disclosing a binodal 6,6-connected bilayer with the **6,6L1** topology and the point symbol (4^{15}). After collisions are removed (nodes with the same neighbors), this net can become simpler, converting to the 3,6-c **kgd** topology.

CaL_2(H_2O). This 1D coordination polymer features an intricate metal−organic chain that is built from 5-connected Ca nodes, 3-connected μ_3-L nodes, and 2-connected μ-L linkers (Figure 18). This chain can be classified as a binodal 3,5-connected net with the **3,5C1** topology and the point symbol $(3.4^2)(3^2.4^2.5^3.6^2.7)$.

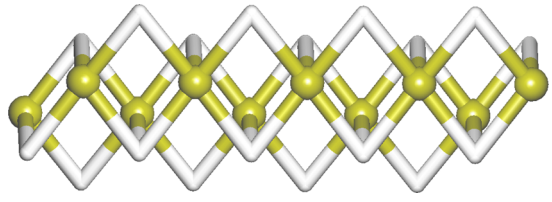

Figure 18. Topological representation of the 1D metal−organic network in CaL_2(H_2O) displaying a binodal 3,5-connected underlying chain with the **3,5C1** topology. View along the *b* axis Color codes: 5-connected Ca nodes (olive balls), centroids of 3- and 2-connected μ_3-L nodes and μ-L linkers (gray). The 2-connected μ-L linkers were not considered for the topological classification (including the calculation of the point symbol).

SrL_2(H_2O) and BaL_2(H_2O). These 2D coordination polymers are also similar, and thus only the structure of SrL_2(H_2O) is described. An underlying network in SrL_2(H_2O) is assembled from the 8-connected Sr nodes, 3-connected μ_3-L nodes, and 2-connected μ-H_2O linkers (Figure 19). This net can be defined as a binodal 3,8-connected layer with the **3,8L28** topology and the point symbol $(3.4^2)_2(3^4.4^3.5^8.6^{12}.7)$. This layer can be simplified further by omitting the μ-H_2O linkers, resulting in a binodal 3,6-connected net with the **3,6L66** topology. Additionally, the **3,8L28** net can be converted to the **sdd** network after removing collisions (nodes with the same neighbors) and then to the **hcb** layer after removing the μ-H_2O linkers.

$CuL_2(H_2O)_7$. This compound is composed of the discrete 0D cyclic dimers $[Cu_2(\mu\text{-}L)_2(L)_2(H_2O)_6]$ that are multiply interlinked by hydrogen bonds to generate a 3D H-bonded

https://doi.org/10.1021/acs.cgd.1c00683
Cryst. Growth Des. 2021, 21, 5421−5439

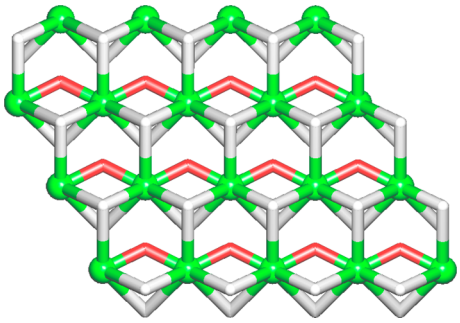

Figure 19. Topological representation of the 2D metal−organic network in $SrL_2(H_2O)$ displaying a binodal 3,8-connected underlying layer with the **3,8L28** topology. View along the *c* axis (slightly rotated). Color codes: Sr nodes, green spheres; centroids of 3-connected μ_3-L nodes, gray; centroids of 2-connected μ-H_2O linkers, red. The 2-connected μ-L linkers were not considered for the topological classification (including the calculation of the point symbol).

framework (Figure 20). It can be described as a uninodal 8-connected net with the **hex** (hexagonal primitive) topology and point symbol ($3^6.4^{18}.5^3.6$).

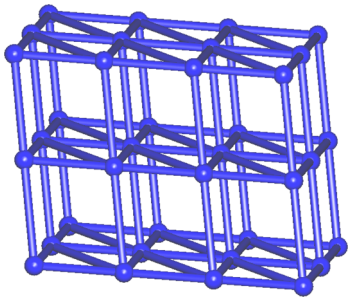

Figure 20. Topological representation of the 3D H-bonded network in $CuL_2(H_2O)_7$ displaying a uninodal 8-connected net with the **hex** topology, View along the *c* axis (slightly rotated). Color codes: centroids of 8-connected $[Cu_2(\mu\text{-}L)_2(L)_2(H_2O)_6]$ molecular nodes, blue spheres.

$CdL_2(H_2O)_5$. As in the case of $CuL_2(H_2O)_7$, the structure of $CdL_2(H_2O)_5$ reveals a similar type of 0D cyclic dimer $[Cd_2(\mu\text{-}L)_2(L)_2(H_2O)_6]$. However, the hydrogen-bonding interactions between the adjacent dicadmium(II) molecular units are slightly different. As a result, a uninodal 6-connected net with the **pcu** (alpha-Po primitive cubic) topology and the point symbol ($4^{12}.6^3$) is generated (Figure 21).

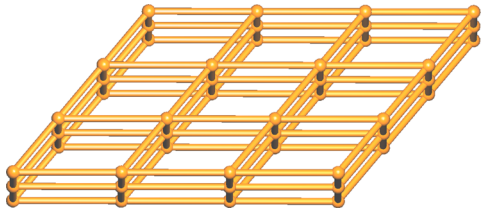

Figure 21. Topological representation of 3D H-bonded network in $CdL_2(H_2O)_5$, displaying a uninodal 6-connected net with the **pcu** topology. View along the *a* axis (slightly rotated). Color codes: centroids of 6-connected $[Cd_2(\mu\text{-}L)_2(L)_2(H_2O)_6]$ molecular nodes, orange spheres.

Thermogravimetric Analysis. $HL{\cdot}H_2O$ shows no weight loss upon heating up to 150 °C (Figure S6). Between 150 and 190 °C, approximately half of the water content is lost (5%). Above this temperature there is no weight loss again up until 285 °C (pyrazole-4-sulfonic acid decomposes at 305 °C). Between 300 and 370 °C, a sharp weight loss of 82% is observed, then more of the residue (up to 90%) is lost slowly on heating to 700 °C. The ammonium salt (NH_4L) is stable up to 90 °C (in comparison to 225 °C for the pyrazole-4-sulfonate salt), when decomposition begins (Figure S7). A weight loss of 3% occurs between 100 and 200 °C. Further weight loss up to a total of 15% is observed at 270 °C. A sharp weight loss up to a total of 77% occurs between 270 and 360 °C. Further weight loss up to a total of 86% is observed on heating to 700 °C. The metal coordination compounds first lose H_2O (unless anhydrous at room temperature), followed by dimethylpyrazole (starting at 200−230 °C) and finally SO_2, leaving behind the corresponding metal sulfates. The observed decomposition temperatures are 55−60 °C lower in comparison to the corresponding pyrazole-4-sulfonate complexes of alkali metals and 5−25 °C lower in the case of alkaline-earth-metal complexes. Details for some individual metal complexes are given below.

$LiL(H_2O)$ is stable up to 100 °C, and then it loses its water content on heating up to 200 °C (Figure S8). Above this temperature it starts decomposing and it loses 48% of its weight up to 360 °C; then it loses more weight (up to 65%) on heating to 700 °C.

$NaL(H_2O)$ starts losing its H_2O molecule at 53 °C (Figure S9). The anhydrous form is stable between 80 and 210 °C. Above this temperature, decomposition occurs and a total weight loss of 53% is observed up to 410 °C. Further weight loss (up to a total of 60%) is observed on heating to 700 °C.

KL is anhydrous at room temperature and is stable up to 210 °C (Figure S10). A weight loss of 36% is observed between 210 and 300 °C, and then further loss to a total of 50% takes place up to 540 °C. The residue is stable between 540 and 700 °C.

CsL is also anhydrous at room temperature and is stable up to 200 °C, then a weight loss of 37% is observed between 200 and 400 °C (Figure S11). Above this temperature further loss to a total of 42% takes place up to 700 °C.

$MgL_2(H_2O)_6$ loses three H_2O molecules between 51 and 69 °C, another two H_2O molecules between 87 and 102 °C, and the sixth H_2O molecule by 152 °C (Figure S12). Further decomposition occurs above this temperature, with a total weight loss of 71% at 370 °C. Further weight loss (up to a total of 75%) is observed on heating to 700 °C.

$CaL_2(H_2O)$ starts losing its H_2O molecule at 90 °C (Figure S13). The anhydrous form is stable between 130 and 230 °C. Above this temperature, decomposition occurs and a total weight loss of 51% is observed up to 450 °C. Further weight loss (up to a total of 56%) is observed on heating to 700 °C.

$SrL_2(H_2O)$ starts losing H_2O at 90 °C and becomes anhydrous at 180 °C (Figure S14). Further decomposition starts at 225 °C, with a total weight loss of 46% at 370 °C. Further weight loss up to a total of 61% is observed on heating to 700 °C.

$BaL_2(H_2O)$ is stable up to 175 °C, when it starts losing H_2O, and becomes anhydrous at 225 °C (Figure S15). At that temperature further decomposition starts taking place, with a total weight loss of 41% at 360 °C. Further weight loss up to a total of 48% is observed on heating to 700 °C.

https://doi.org/10.1021/acs.cgd.1c00683
Cryst. Growth Des. 2021, 21, 5421−5439

Efficiency of HL and Metal−L Compounds in Copper Corrosion Inhibition. The corrosion inhibition efficiency of the materials described herein was quantified as the "corrosion rate" (CR), by using the equation

$$\mathrm{CR} = 87.6 \times \frac{\text{mass loss}}{(\text{area})(\text{time})(\text{metal density})}$$

The units: are CR in mm/year, mass loss in mg, area in cm^2, time in hours, and metal density = 8.94 g/cm^3 (for Cu).

On the basis of previous studies,[41,42] the pyrazole-4-sulfonate anion is not effective in inhibiting copper corrosion at pH 2 (its CR is 0.45 mm/year, the same as the "control"), but it does decrease corrosion significantly at higher pH values. At pH 3, for example, a CR of 0.05 mm/year is measured in the presence of pyrazole-4-sulfonate, in comparison to 0.31 mm/year in the absence of pyrazole-4-sulfonate ("control").

In the present study we used the corrosion inhibitor HL, as well as several of its derivatives with monovalent (NH_4^+, Li^+, Na^+, K^+, Cs^+) and divalent (Mg^{2+}, Ca^{2+}, Sr^{2+}, Ba^{2+}) cations. The corrosion inhibition results at pH values of 2, 3, and 4 are shown in Figure 22.

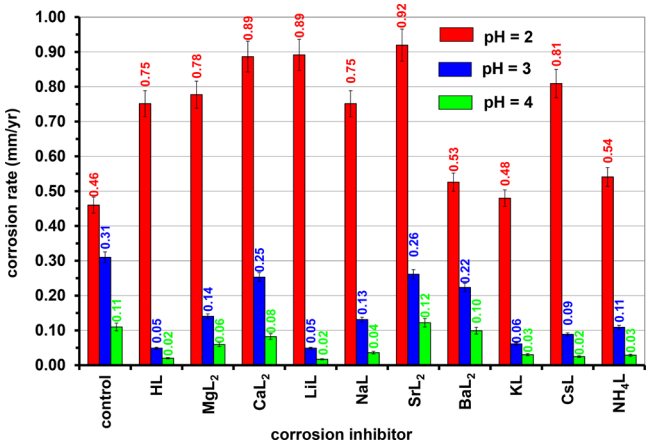

Figure 22. Copper corrosion rates at pH 2 (red), 3 (blue) and 4 (green). Dotted lines represent the "control" corrosion rates and are added to facilitate comparisons.

The first observation is that as the pH is increased, corrosion rates decrease. This is true in the absence (control) or presence of inhibitor additives and has been observed in the literature.[80−86] A drop in the CR of the "control" from 0.46 to 0.31 mm/year upon increasing the pH from 2 to 3 is observed. A further drop in the CR of the "control" is observed on going from pH 3 to 4 (0.11 mm/year). In the presence of any additive, CRs increase at pH 2. The highest increase is observed for the SrL additive, 0.92 mm/year, while the lowest increase is noted for the KL additive, 0.48 mm/year. When the solution pH is increased to 3, all CRs in the presence of additives are lower than that of the control. The CR in the presence of SrL is 0.26 mm/year (a 16% decrease), while in the presence of LiL it is 0.05 mm/year (a 84% decrease). Finally, at pH 4, the most effective corrosion inhibitors are HL, LiL, and CsL with CRs of 0.02 mm/year (a 82% decrease). NaL, MgL and NH_4L also show good inhibition capabilities.

For each experiment, the copper surfaces were photographed after removal from the corresponding solutions. Images from the experiments at pH 3 and 4 are shown in Figure 23. In all of them, the presence of copper oxide is evident, due to incomplete inhibition of the corrosion process.

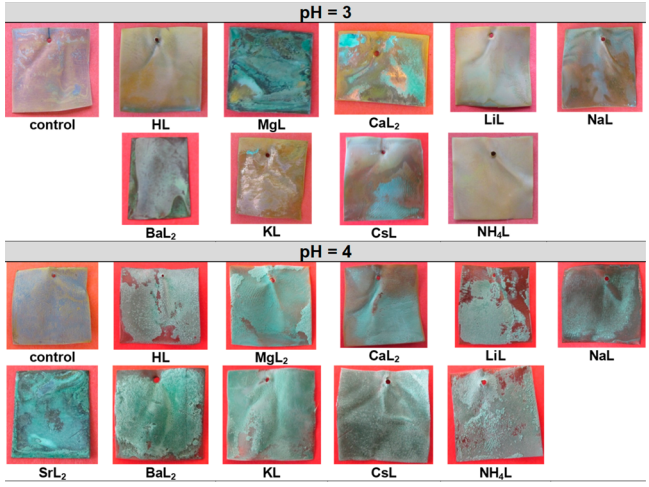

Figure 23. Selected images of unprotected (control) and protected surfaces at pH 3 and 4.

Study of Protective Films. Copper specimens were also studied by scanning electron microscopy and energy dispersive X-ray spectroscopy (SEM/EDS). EDS has successfully been used previously in anticorrosion coating composition studies.[80−86] Figure 24 shows representative SEM images of the anticorrosion protective films studied here at pH 3 and 4. The "control" specimen had a continuous crystalline film of copper oxide (identified by EDS), visible by both optical microphotography and SEM (see image "control"). In the presence of HL (see image "HL"), the surface morphology reveals a much smoother film at pH 3 but presents aggregated particles at pH 4, presumably due to HL deposition/crystallization on the copper surface. The protective films formed by metal−L additives appear very rough, with discontinuous surface coverage and obvious particle formation on the surface. Different particle morphologies most likely represent the individual crystalline aggregates formed for each derivative. EDS of selected specimens revealed the presence of the respective cation and L used in each experiment, thus confirming the formation of metal−L protective films.

CONCLUSIONS

Similarly to pyrazole-4-sulfonate, 3,5-dimethylpyrazole-4-sulfonate (L^-) forms layered inorganic−organic constructs with metal ions in the solid state, with the exception of the Cu^{2+} structure, which does not have a layered structure. The molecular and supramolecular structures of the metal−L coordination compounds, however, are significantly different from those of the corresponding parent pyrazole-4-sulfonate complexes. Indeed, the two methyl substituents of L^- induce changes in both the organic and inorganic layers of the coordination compounds. The origin of the differences is the inability of the 3,5-dimethylpyrazole aromatic rings to form efficient edge-to-face or stacking interactions within the organic layer. While edge-to-face (or strong $\pi-\pi$ stacking) aromatic interactions are present in most known pyrazole-4-sulfonate complexes, a herringbone pattern with methyl C−H···π interactions and long pyrazole centroid···centroid distances of 5.28−5.96 Å is observed in the coordination

https://doi.org/10.1021/acs.cgd.1c00683
Cryst. Growth Des. 2021, 21, 5421−5439

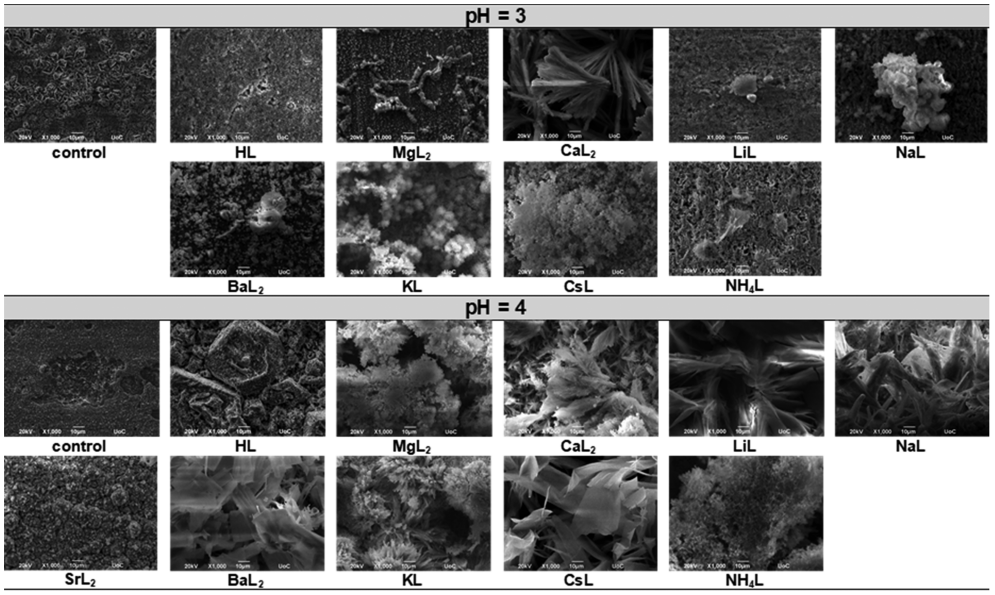

Figure 24. SEM images of protective films on copper surfaces at pH 3 and 4.

polymers of L with Li, Na, Rb, Cs, Ca, Sr, and Ba (in comparison to 3.49−3.76 Å in the corresponding pyrazole-4-sulfonate derivatives). Also, the organic layer is almost twice as thick in the case of coordination polymers of L, due to the intraorganic-layer N−H···N hydrogen bonding between pyrazole units (as opposed to N−H···O hydrogen bonding to sulfonate groups). The effect of the methyl substituents is felt in the inorganic layer as well, wherein the metal ions have different coordination numbers and hydration degrees in comparison to the pyrazole-4-sulfonate analogues.

A topological classification of the obtained compounds reveals a number of distinct topological nets, including some rare examples.[76−79,87,88] Thus, the present work shows that 3,5-dimethylpyrazole-4-sulfonate is a versatile building block for the construction of a wide variety of alkali-, alkaline-earth-, and transition-metal coordination polymers.

Copper corrosion experiments show that, at pH 4, the free 3,5-dimethylpyrazole-4-sulfonic acid (HL) is a better anticorrosion agent than the parent pyrazole-4-sulfonic acid. However, the metal complexes of L^- offer weaker corrosion protection than the corresponding pyrazole-4-sulfonate derivatives. This might be attributed to two different factors. First, structural studies revealed that the films formed by metal−L complexes are less compact than the corresponding films with pyrazole-4-sulfonate. Second, because HL is a weaker acid (pK_a 1.06) than pyrazole-4-sulfonic acid (pK_a = −0.04), L^- is more easily protonated in the metal−L coordination compounds, rendering the protective films less robust. We are currently studying pyrazole-4-sulfonate derivatives with substituents that enhance aromatic $\pi-\pi$ interactions, which are expected to lead to improved anticorrosion performance.

■ ASSOCIATED CONTENT

Supporting Information

The Supporting Information is available free of charge at https://pubs.acs.org/doi/10.1021/acs.cgd.1c00683.

NMR spectrum of HL, details of the pK_a measurements, and thermogravimetric analysis data (PDF)

Accession Codes

CCDC 2088836 and 2088838−2088846 contain the supplementary crystallographic data for this paper. These data can be obtained free of charge via www.ccdc.cam.ac.uk/data_request/cif, or by emailing data_request@ccdc.cam.ac.uk, or by contacting The Cambridge Crystallographic Data Centre, 12 Union Road, Cambridge CB2 1EZ, UK; fax: +44 1223 336033.

■ AUTHOR INFORMATION

Corresponding Authors

Gellert Mezei − *Department of Chemistry, Western Michigan University, Kalamazoo, Michigan 49008, United States;* orcid.org/0000-0002-3120-3084; Email: gellert.mezei@wmich.edu

Konstantinos D. Demadis − *Crystal Engineering, Growth and Design Laboratory, Department of Chemistry, University of Crete, Voutes Campus, Heraklion, Crete GR-71003, Greece;* orcid.org/0000-0002-0937-8769; Email: demadis@uoc.gr

Authors

Wisam A. Al Isawi − *Department of Chemistry, Western Michigan University, Kalamazoo, Michigan 49008, United States*

Sarut Jianrattanasawat − *Department of Chemistry, Western Michigan University, Kalamazoo, Michigan 49008, United States*

Eleftherios Tripodianos − *Crystal Engineering, Growth and Design Laboratory, Department of Chemistry, University of Crete, Voutes Campus, Heraklion, Crete GR-71003, Greece*

Alexander M. Kirillov − *Centro de Química Estrutural and Departamento de Engenharia Química, Instituto Superior Técnico, Universidade de Lisboa, 1049-001 Lisbon, Portugal; Research Institute of Chemistry, Peoples' Friendship University of Russia (RUDN University), Moscow 117198, Russia*

Matthias Zeller − *Department of Chemistry, Purdue University, West Lafayette, Indiana 47907, United States;* orcid.org/0000-0002-3305-852X

Complete contact information is available at:

https://doi.org/10.1021/acs.cgd.1c00683
Cryst. Growth Des. 2021, 21, 5421−5439

https://pubs.acs.org/10.1021/acs.cgd.1c00683

Notes

The authors declare no competing financial interest.

■ ACKNOWLEDGMENTS

This material is based on work supported by the National Science Foundation under Grant No. CHE-1808554 (G.M.). A.M.K. acknowledges the FCT (LISBOA-01-0145-FEDER-029697) and RUDN University (Strategic Academic Leadership Program).

■ REFERENCES

(1) www.mineralseducationcoalition.org/mining-minerals-information/mining-mineral-statistics (accessed 06/08/2021).
(2) Georgiadou, M.; Alkire, R. Modelling of Copper Etching in Aerated Chloride Solutions. *J. Appl. Electrochem.* **1997**, *28*, 127−134.
(3) Arjmand, F.; Adriaens, A. Influence of pH and Chloride Concentration on the Corrosion Behavior of Unalloyed Copper in NaCl Solution: A Comparative Study between the Micro and Macro Scales. *Materials* **2012**, *5*, 2439−2464.
(4) Federal Highway Administration (FHWA), Office of Infrastructure Research and Development, report FHWA-RD-01-156: Corrosion Cost and Preventive Strategies in the United States, 2001.
(5) Shinato, K. W.; Zewde, A. A.; Jin, Y. Corrosion Protection of Copper and Copper Alloys in Different Corrosive Medium Using Environmentally Friendly Corrosion Inhibitors. *Corros. Rev.* **2020**, *38*, 101−109.
(6) Ibrahim, M. M.; Saleh, D. I.; El-Hendawy, M. M.; Fallatah, A. M.; Mersal, G. A. M.; Boukherroub, R.; Wysocka, J.; Ryl, J.; Amin, M. A. Efficacious Alkaline Copper Corrosion Inhibition by a Mixed Ligand Copper(II) Complex of 2,2′-Bipyridine and Glycine: Electrochemical and Theoretical Studies. *ChemElectroChem* **2021**, *8*, 2052−2064.
(7) Neupane, S.; Losada-Pérez, P.; Tiringer, U.; Taheri, P.; Desta, D.; Xie, C.; Crespo, D.; Mol, A.; Milošev, I.; Kokalj, A.; Renner, F. U. Study of Mercaptobenzimidazoles as Inhibitors for Copper Corrosion: Down to the Molecular Scale. *J. Electrochem. Soc.* **2021**, *168*, 051504.
(8) Rizvi, M.; Gerengi, H.; Kaya, S.; Uygur, I.; Yildiz, M.; Sarioglu, I.; Cingiz, Z.; Mielniczek, M.; El Ibrahimi, B. Sodium Nitrite as a Corrosion Inhibitor of Copper in Simulated Cooling Water. *Sci. Rep.* **2021**, *11*, 8353.
(9) Simonović, A. T.; Tasić, Z. Z.; Radovanović, M. B.; Petrović Mihajlović, M. B.; Antonijević, M. M. Influence of 5-Chlorobenzotriazole on Inhibition of Copper Corrosion in Acid Rain Solution. *ACS Omega* **2020**, *5*, 12832−12841.
(10) Chukwuike, V. I.; Prasannakumar, R. S.; Gnanasekar, K.; Barik, R. C. Copper corrosion mitigation: A New Insight for Fabricating a Surface Barrier Film Against Chloride Ion Under Hydrodynamic Flow. *Appl. Surf. Sci.* **2021**, *555*, 149703.
(11) Sharma, S. B.; Maurice, V.; Klein, L. H.; Marcus, P. *In Situ* Scanning Tunneling Microscopy Study of 2-Mercaptobenzimidazole Local Inhibition Effects on Copper Corrosion at Grain Boundary Surface Terminations. *Electrochim. Acta* **2021**, *378*, 138150.
(12) Zhang, F.; Örnek, C.; Liu, M.; Müller, T.; Lienerc, U.; Ratia-Hanby, V.; Carpén, L.; Isotahdon, E.; Pan, J. Corrosion-Induced Microstructure Degradation of Copper in Sulfide-Containing Simulated Anoxic Groundwater Studied by Synchrotron High-Energy X-ray Diffraction and *ab-initio* Density Functional Theory Calculation. *Corros. Sci.* **2021**, *184*, 109390.
(13) Qiu, S.; Su, Y.; Zhao, H.; Wang, L.; Xue, Q. Ultrathin Metal-Organic Framework Nanosheets Prepared via Surfactant-Assisted Method and Exhibition of Enhanced Anticorrosion for Composite Coatings. *Corros. Sci.* **2021**, *178*, 109090.
(14) Tao, Z.; Liu, G.; Li, Y.; Zhang, R.; Su, H.; Li, S. Electrochemical Investigation of Tetrazolium Violet as a Novel Copper Corrosion Inhibitor in an Acid Environment. *ACS Omega* **2020**, *5*, 4415−4423.
(15) Zhang, K.; Lu, J.; Li, J.; Zhang, D.; Gao, L.; Zhou, H. An Improved Approach to Prepare Triazole Protective Film by Click-Assembly on Copper Surface. *Corros. Sci.* **2020**, *164*, 108352.
(16) Schindelholz, E. J.; Spoerke, E. D.; Nguyen, H.-D.; Grunlan, J. C.; Qin, S.; Bufford, D. C. Extraordinary Corrosion Protection from Polymer−Clay Nanobrick Wall Thin Films. *ACS Appl. Mater. Interfaces* **2018**, *10*, 21799−21803.
(17) Fateh, A.; Aliofkhazraei, M.; Rezvanian, A. R. Review of Corrosive Environments for Copper and its Corrosion Inhibitors. *Arabian J. Chem.* **2020**, *13*, 481−544.
(18) Finšgar, M.; Milošev, I. Inhibition of Copper Corrosion by 1,2,3-Benzotriazole: A Review. *Corros. Sci.* **2010**, *52*, 2737−2749.
(19) Antonijevic, M. M.; Petrovic, M. B. Copper Corrosion Inhibitors. A Review. *Int. J. Electrochem. Sci.* **2008**, *3*, 1−28.
(20) Mathiyarasu, J.; Pathak, S. S.; Yegnaraman, V. Review on Corrosion Prevention of Copper Using Ultrathin Organic Monolayers. *Corros. Rev.* **2006**, *24*, 307−322.
(21) Vastag, Gy; Szöcs, E.; Shaban, A.; Kálmán, E. New Inhibitors for Copper Corrosion. *Pure Appl. Chem.* **2001**, *73*, 1861−1869.
(22) Magnussen, O. M.; Behm, R. J. Atomic-Scale Processes in Cu Corrosion and Corrosion Inhibition. *MRS Bull.* **1999**, *24*, 16−23.
(23) Allam, N. K.; Nazeer, A. A.; Ashour, E. A. A Review of the Effects of Benzotriazole on the Corrosion of Copper and Copper Alloys in Clean and Polluted Environments. *J. Appl. Electrochem.* **2009**, *39*, 961−969.
(24) Antonijevic, M. M.; Milic, S. M.; Petrovic, M. B. Films Formed on Copper Surface in Chloride Media in the Presence of Azoles. *Corros. Sci.* **2009**, *51*, 1228−1237.
(25) Lee, J.-W.; Kang, M.-C.; Kim, J. J. Characterization of 5-Aminotetrazole as a Corrosion Inhibitor in Copper Chemical Mechanical Polishing. *J. Electrochem. Soc.* **2005**, *152*, C827−C831.
(26) Kokalj, A.; Kovačević, N.; Peljhan, S.; Finšgar, M.; Lesar, A.; Milošev, I. Triazole, Benzotriazole, and Naphthotriazole as Copper Corrosion Inhibitors: I. Molecular Electronic and Adsorption Properties. *ChemPhysChem* **2011**, *12*, 3547−3555.
(27) Kovačević, N.; Kokalj, A. The Relation Between Adsorption Bonding and Corrosion Inhibition of Azole Molecules on Copper. *Corros. Sci.* **2013**, *73*, 7−17.
(28) Kovačević, N.; Milošev, I.; Kokalj, A. How Relevant is the Adsorption Bonding of Imidazoles and Triazoles for their Corrosion Inhibition of Copper? *Corros. Sci.* **2017**, *124*, 25−34.
(29) Kovačević, N.; Kokalj, A. DFT Study of Interaction of Azoles with Cu(111) and Al(111) Surfaces: Role of Azole Nitrogen Atoms and Dipole−Dipole Interactions. *J. Phys. Chem. C* **2011**, *115*, 24189−24197.
(30) Kokalj, A.; Peljhan, S.; Finšgar, M.; Milošev, I. What Determines the Inhibition Effectiveness of ATA, BTAH, and BTAOH Corrosion Inhibitors on Copper? *J. Am. Chem. Soc.* **2010**, *132*, 16657−16668.
(31) Ofoegbu, S. U.; Galvão, T. L. P.; Gomes, J. R. B.; Tedim, J.; Nogueira, H. I. S.; Ferreira, M. G. S.; Zheludkevich, M. L. Corrosion Inhibition of Copper in Aqueous Chloride Solution by 1*H*-1,2,3-Triazole and 1,2,4-Triazole and their Combinations: Electrochemical, Raman and Theoretical Studies. *Phys. Chem. Chem. Phys.* **2017**, *19*, 6113−6129.
(32) Jiang, L.; Lan, Y.; He, Y.; Li, Y.; Li, Y.; Luo, J. 1,2,4-Triazole as a Corrosion Inhibitor in Copper Chemical Mechanical Polishing. *Thin Solid Films* **2014**, *556*, 395−404.
(33) Törnkvist, C.; Thierry, D.; Bergman, J.; Liedberg, B.; Leygraf, C. Methyl Substitution in Benzotriazole and Its Influence on Surface Structure and Corrosion Inhibition. *J. Electrochem. Soc.* **1989**, *136*, 58−64.
(34) Chen, X.; Häkkinen, H. Divide and Protect: Passivating Cu(111) by Cu-$(benzotriazole)_2$. *J. Phys. Chem. C* **2012**, *116*, 22346−22349.
(35) Saavedra-Torres, M.; Escobar, C. A.; Ocayo, F.; Tielens, F.; Santos, J. C. 1,2,3-Benzotriazole Derivatives Adsorption on Cu(1 1 1) Surface: A DFT Study. *Chem. Phys. Lett.* **2017**, *689*, 128−134.

(36) Gong, Y.; Wang, Z.; Gao, F.; Zhang, S.; Li, H. Synthesis of New Benzotriazole Derivatives Containing Carbon Chains as the Corrosion Inhibitors for Copper in Sodium Chloride Solution. *Ind. Eng. Chem. Res.* **2015**, *54*, 12242−12253.
(37) Grillo, F.; Tee, D. W.; Francis, S. M.; Früchtl, H. A.; Richardson, N. V. Passivation of Copper: Benzotriazole Films on Cu(111). *J. Phys. Chem. C* **2014**, *118*, 8667−8675.
(38) Cang, H.; Shi, W.; Shao, J.; Xu, Q. Study on the Pyrazole Corrosion Inhibition and Synergistic Effect for Copper in Alkaline Solution. *Int. J. Electrochem. Sci.* **2012**, *7*, 5626−5632.
(39) Geler, E.; Azambuja, D. S. Corrosion Inhibition of Copper in Chloride Solutions by Pyrazole. *Corros. Sci.* **2000**, *42*, 631−643.
(40) Goswami, A.; Koskey, S.; Mukherjee, T.; Chyan, O. Study of Pyrazole as Copper Corrosion Inhibitor in Alkaline Post Chemical Mechanical Polishing Cleaning Solution. *ECS J. Solid State Sci. Technol.* **2014**, *3*, P293−P297.
(41) Fernando, I. R.; Daskalakis, N.; Demadis, K. D.; Mezei, G. Cation Effect on the Inorganic−Organic Layered Structure of Pyrazole-4-Sulfonate Networks and Inhibitory Effects on Copper Corrosion. *New J. Chem.* **2010**, *34*, 221−235.
(42) Fernando, I. R.; Jianrattanasawat, S.; Daskalakis, N.; Demadis, K. D.; Mezei, G. Mapping the Supramolecular Chemistry of Pyrazole-4-Sulfonate: Layered Inorganic−Organic Networks with Zn^{2+}, Cd^{2+}, Ag^{+}, Na^{+} and NH_4^{+}, and their Use in Copper Anticorrosion Protective Films. *CrystEngComm* **2012**, *14*, 908−919.
(43) Babic-Samardzija, K.; Lupu, C.; Hackerman, N.; Barron, A. R.; Luttge, A. Inhibitive Properties and Surface Morphology of a Group of Heterocyclic Diazoles as Inhibitors for Acidic Iron Corrosion. *Langmuir* **2005**, *21*, 12187−12196.
(44) Côté, A. P.; Shimizu, G. K. H. The Supramolecular Chemistry of the Sulfonate Group in Extended Solids. *Coord. Chem. Rev.* **2003**, *245*, 49−64.
(45) Shimizu, G. K. H.; Vaidhyanathan, R.; Taylor, J. M. Phosphonate and Sulfonate Metal Organic Frameworks. *Chem. Soc. Rev.* **2009**, *38*, 1430−1449.
(46) Shimizu, G. K. H.; Taylor, J. M.; Vaidhyanathan, R. Supramolecular Coordination Networks Employing Sulfonate and Phosphonate Linkers: From Layers to Open Structures. In *Macromolecules Containing Metal and Metal-Like Elements*; Abd-El Aziz, A. S., Carraher, C. E., Jr., Pittman, C. U., Jr., Zeldin, M., Eds.; Wiley: 2009; Vol. *9*.
(47) Zhang, G.; Fei, H. Synthesis and Applications of Porous Organosulfonate-Based Metal−Organic Frameworks. *Top. Curr. Chem.* **2019**, *377*, 32.
(48) Zhang, G.; Wei, G.; Liu, Z.; Oliver, S. R. J.; Fei, H. A Robust Sulfonate-Based Metal−Organic Framework with Permanent Porosity for Efficient CO_2 Capture and Conversion. *Chem. Mater.* **2016**, *28*, 6276−6281.
(49) Desai, A. V.; Joarder, B.; Roy, A.; Samanta, P.; Babarao, R.; Ghosh, S. K. Multifunctional Behavior of Sulfonate-Based Hydrolytically Stable Microporous Metal−Organic Frameworks. *ACS Appl. Mater. Interfaces* **2018**, *10*, 39049−39055.
(50) Yu, Y.-Z.; Li, Y.-N.; Deng, Z.-P.; Zhu, Z.-B.; Huo, L.-H.; Gao, S. Influence of Metal Cations and Coordination Modes on Luminescent Group 1 and 2 Metal Sulfonate Complexes Constructed from 4,4′-Dihydroxybiphenyl-3,3′-disulfonic Acid. *Eur. J. Inorg. Chem.* **2015**, *2015*, 2254−2263.
(51) Zhu, Z.-B.; Wan, W.; Deng, Z.-P.; Ge, Z.-Y.; Huo, L.-H.; Zhao, H.; Gao, S. Structure Modulations in Luminescent Alkaline Earth Metal-Sulfonate Complexes Constructed from Dihydroxyl-1,5-Benzenedisulfonic Acid: Influences of Metal Cations, Coordination Modes and pH Value. *CrystEngComm* **2012**, *14*, 6675−6688.
(52) Kennedy, A. R.; Andrikopoulos, P. C.; Arlin, J.-B.; Armstrong, D. R.; Duxbury, N.; Graham, D. V.; Kirkhouse, J. B. A. Supramolecular Structure in s-Block Metal Complexes of Sulfonated Monoazo Dyes: Discrepant Packing and Bonding Behavior of *ortho*-Sulfonated Azo Dyes. *Chem. - Eur. J.* **2009**, *15*, 9494−9504.
(53) Astbury, C.; Conway, L. K.; Gillespie, C.; Hodge, K.; Innes, E.; Kennedy, A. R. A Structural Study of Seven Salt Forms of Sulfonated Azo Dyes Containing Nitrile Functional Groups. *Dyes Pigm.* **2013**, *97*, 100−104.
(54) Gardner, H. C.; Kennedy, A. R.; McCarney, K. M.; Staunton, E.; Stewart, H.; Teat, S. J. Structures of Five Salt Forms of Disulfonated Monoazo Dyes. *Acta Crystallogr., Sect. C: Struct. Chem.* **2020**, *C76*, 972−981.
(55) Kennedy, A. R.; Conway, L. K.; Kirkhouse, J. B. A.; McCarney, K. M.; Puissegur, O.; Staunton, E.; Teat, S. J.; Warren, J. E. Monosulfonated Azo Dyes: A Crystallographic Study of the Molecular Structures of the Free Acid, Anionic and Dianionic Forms. *Crystals* **2020**, *10*, 662.
(56) Kennedy, A. R.; Kirkhouse, J. B. A.; Whyte, L. Supramolecuar Motifs in s-Block Metal-Bound Sulfonated Monoazo Dyes: The Case of Orange G. *Inorg. Chem.* **2006**, *45*, 2965−2971.
(57) Grandberg, I. I.; Nam, N. L.; Sorokin, V. I. New Method for the Sulfonation of Pyrazoles. *Chem. Heterocycl. Compd.* **1997**, *33*, 532−534.
(58) Jianrattanasawat, S.; Mezei, G. 3,5-Dimethylpyrazole Promoted Sulfonation of Acetic Anhydride by H_2SO_4 to Sulfoacetic Acid and Methanedisulfonic Acid, and Crystal Structures of the Complexes with Co^{2+}, Zn^{2+}, Ba^{2+}, Pb^{2+} and Cs^{+}. *Inorg. Chim. Acta* **2012**, *384*, 318−323.
(59) Morgan, G. T.; Ackerman, I. CLII.−Substitution in the Pyrazole Series. Halogen Derivatives of 3:5-Dimethylpyrazole. *J. Chem. Soc., Trans.* **1923**, *123*, 1308−1318.
(60) Koeberg-Telder, A.; Cerfontain, H. Solutes in Sulphuric Acid. Part VI. A Nuclear Magnetic Resonance Study of Organic Sulphonic Acids and ^{1}H Nuclear Magnetic Resonance Standards; pK_{BH} Determination of Sulphonic Acids. *J. Chem. Soc., Perkin Trans. 2* **1975**, 226−229.
(61) Lee, D. G. Determination of pK_{BH}+ for Aliphatic Ketones from Nuclear Magnetic Resonance Chemical Shift Data. *Can. J. Chem.* **1970**, *48*, 1919−1923.
(62) Yates, K.; Stevens, J. B.; Katritzky, A. R. The Ionization Behavior of Amides in Concentrated Sulphuric Acids: I. A New Acidity Function Based on a Set of Primary Amide Indicators. *Can. J. Chem.* **1964**, *42*, 1957−1970.
(63) Bascombe, K. N.; Bell, R. P. Acidity Functions of Some Aqueous Acids. *J. Chem. Soc.* **1959**, 1096−1104.
(64) NACE Standard TM0169-95 (Item No. 21200), National Association of Corrosion Engineers, Houston TX, U.S.A. (www.nace.org).
(65) *SAINT v.8.38A*; Bruker: 2017.
(66) Krause, L.; Herbst-Irmer, R.; Sheldrick, G. M.; Stalke, D. Comparison of Silver and Molybdenum Microfocus X-Ray Sources for Single-Crystal Structure Determination. *J. Appl. Crystallogr.* **2015**, *48*, 3−10.
(67) Sheldrick, G. M. *TWINABS 2012/1*; Bruker: 2012.
(68) Sheldrick, G. M. A Short History of *SHELX*. *Acta Crystallogr., Sect. A: Found. Crystallogr.* **2008**, *A64*, 112−122.
(69) Sheldrick, G. M. Crystal Structure Refinement with *SHELXL*. *Acta Crystallogr., Sect. C: Struct. Chem.* **2015**, *C71*, 3−8.
(70) Sheldrick, G. M. *CELL_NOW*; Georg-August-Universität: 2008.
(71) Mezei, G.; Raptis, R. G. Pyrazole-4-Sulfonate Networks of Alkali and Alkaline-Earth Metals. Effect of Cation Size, Charge, H-bonding and Aromatic Interactions on the Three-Dimensional Supramolecular Architecture. *New J. Chem.* **2003**, *27*, 1399−1407.
(72) Desiraju, G. R. Designer Crystals: Intermolecular Interactions, Network Structures and Supramolecular Synthons. *Chem. Commun.* **1997**, 1475−1482.
(73) Ardizzoia, G. A.; Brenna, S.; Civati, F.; Colombo, V.; Sironi, A. A Phosphorescent Copper(I) Coordination Polymer with Sodium 3,5-Dimethyl-4-Sulfonate Pyrazolate. *CrystEngComm* **2017**, *19*, 6020−6027.
(74) Brenna, S.; Ardizzoia, G. A.; Colombo, V.; Sironi, A. A Silver(I) Coordination Polymer with Sodium 3,5-Dimethyl-4-Sulfonate Pyrazolate: A Nice Example of PXRD Structure Solution and Time-Driven Crystallization. *CrystEngComm* **2019**, *21*, 4586−4592.

https://doi.org/10.1021/acs.cgd.1c00683
Cryst. Growth Des. 2021, 21, 5421−5439

(75) Shannon, R. D. Revised Effective Ionic Radii and Systematic Studies of Interatomic Distances in Halides and Chalcogenides. *Acta Crystallogr., Sect. A: Cryst. Phys., Diffr., Theor. Gen. Crystallogr.* **1976**, *A32*, 751−767.
(76) Blatov, V. A. Multipurpose Crystallochemical Analysis with the Program Package TOPOS. *IUCr CompComm Newsletter* **2006**, *7*, 4−38.
(77) Blatov, V. A.; Shevchenko, A. P.; Proserpio, D. M. Applied Topological Analysis of Crystal Structures with the Program Package ToposPro. *Cryst. Growth Des.* **2014**, *14*, 3576−3586.
(78) O'Keeffe, M.; Yaghi, O. M. Deconstructing the Crystal Structures of Metal−Organic Frameworks and Related Materials into Their Underlying Nets. *Chem. Rev.* **2012**, *112*, 675−702.
(79) Steiner, T. The Hydrogen Bond in the Solid State. *Angew. Chem., Int. Ed.* **2002**, *41*, 48−76.
(80) Demadis, K. D.; Papadaki, M.; Raptis, R. G.; Zhao, H. Corrugated, Sheet-Like Architectures in Layered Alkaline-Earth Metal *R,S*-Hydroxyphosphonoacetate Frameworks: Applications for Anti-corrosion Protection of Metal Surfaces. *Chem. Mater.* **2008**, *20*, 4835−4846.
(81) Demadis, K. D.; Papadaki, M.; Raptis, R. G.; Zhao, H. 2D and 3D Alkaline Earth Metal Carboxyphosphonate Hybrids: Anti-Corrosion Coatings for Metal Surfaces. *J. Solid State Chem.* **2008**, *181*, 679−683.
(82) Demadis, K. D.; Papadaki, M.; Cisarova, I. Single-Crystalline Thin Films by a Rare Molecular Calcium Carboxyphosphonate Trimer Offer Prophylaxis from Metallic Corrosion. *ACS Appl. Mater. Interfaces* **2010**, *2*, 1814−1816.
(83) Demadis, K. D.; Lykoudis, P.; Raptis, R. G.; Mezei, G. Phosphonopolycarboxylates as Chemical Additives for Calcite Scale Dissolution and Metallic Corrosion Inhibition Based on a Calcium-Phosphonotricarboxylate Organic−Inorganic Hybrid. *Cryst. Growth Des.* **2006**, *6*, 1064−1067.
(84) Demadis, K. D.; Mantzaridis, C.; Lykoudis, P. Effects of Structural Differences on Metallic Corrosion Inhibition by Metal−Polyphosphonate Thin Films. *Ind. Eng. Chem. Res.* **2006**, *45*, 7795−7800.
(85) Demadis, K. D.; Barouda, E.; Raptis, R. G.; Zhao, H. Metal Tetraphosphonate "Wires" and Their Corrosion Inhibiting Passive Films. *Inorg. Chem.* **2009**, *48*, 819−821.
(86) Demadis, K. D.; Barouda, E.; Stavgianoudaki, N.; Zhao, H. Inorganic−Organic Hybrid Molecular Ribbons Based on Chelating/Bridging, "Pincer" Tetraphosphonates, and Alkaline-Earth Metals. *Cryst. Growth Des.* **2009**, *9*, 1250−1253.
(87) O'Keeffe, M.; Peskov, M. A.; Ramsden, S. J.; Yaghi, O. M. The Reticular Chemistry Structure Resource (RCSR) Database of, and Symbols for, Crystal Nets. *Acc. Chem. Res.* **2008**, *41*, 1782−1789.
(88) Allen, F. H. The Cambridge Structural Database: A Quarter of a Million Crystal Structures and Rising. *Acta Crystallogr., Sect. B: Struct. Sci.* **2002**, *B58*, 380−388.

https://doi.org/10.1021/acs.cgd.1c00683
Cryst. Growth Des. 2021, 21, 5421−5439